



Ordered mesoporous “one-pot” synthesized Ni-Mg(Ca)-Al₂O₃ as effective and remarkably stable catalysts for combined steam and dry reforming of methane (CSDRM)

Karam Jabbour ^{a,b}, Pascale Massiani ^{a,c,*}, Anne Davidson ^a, Sandra Casale ^a, Nissrine El Hassan ^{b, **}

^a Sorbonne Universités, UPMC Université Paris 06, Laboratoire de Réactivité de Surface, 4 Place Jussieu, 75005 Paris, France

^b Department of Chemical Engineering, Faculty of Engineering, University of Balamand, P.O. Box 33, Amioun, El Koura, Lebanon

^c CNRS UMR 7197, UPMC, Laboratoire de Réactivité de Surface, 4 Place Jussieu, 75005 Paris, France



ARTICLE INFO

Article history:

Received 8 May 2016

Received in revised form 28 July 2016

Accepted 3 August 2016

Available online 4 August 2016

Keywords:

Combined steam and dry reforming (CSDRM)

Metgas

Mesoporous nickel-alumina catalysts

“One-pot” synthesis

MgO

ABSTRACT

Two series of Ni_x% (x: 5–10 wt%) and Ni₅%M₅% (M: Ca or Mg) containing mesoporous Al₂O₃ catalysts were prepared by “one-pot” synthesis following an evaporation-induced self-assembly (EISA) method. After reduction, the catalysts showed very high Ni dispersion within the structured oxide matrix giving high activities and long-term stabilities in combined steam and dry reforming of methane (CSDRM) carried out at 800 °C. Both the increase of Ni content and the addition of Mg (or Ca) are beneficial to performances, with activity levels reaching the maximum-expected thermodynamic ones for Ni₁₀%Al₂O₃. In the Mg (or Ca) free catalysts, a relationship between nickel content, reactivity level and carbon deposition is found. Nevertheless, carbon formation is not detrimental to catalytic stability due to formation of carbon nanotubes only outside the nickel containing alumina grains. Addition of Ca or Mg suppresses to a great extent carbon deposition and leads to high selectivity towards the targeted CSDRM reaction, with almost no occurrence of side reactions. The remarkable thermal stability of the ordered-mesoporous alumina structure (along 40 h of run) along with the stabilization of well-dispersed Ni⁰ within the alumina matrix are shown to be key factors accounting for the excellent long term catalytic performances in spite of the harsh conditions (temperature and steam) imposed by the reaction

© 2016 Elsevier B.V. All rights reserved.

1. Introduction

The excessive emission of large quantities of CO₂ (important anthropogenic greenhouse gas) upon industrial combustion of fossil fuels (natural gas, coal and oil) and its uncontrollable impact on global warming represent nowadays a worldwide concern [1]. While it is essential to reduce greenhouse gases, it is also of strong interest to find routes to transform them into valuable products. At present, a relevant technology resides in the transformation of carbon dioxide to molecules having industrial added values. Amongst such technologies, great attention is focused on the production of synthesis gas (syngas, gaseous mixture of CO and H₂) that constitutes a versatile building block for subsequent produc-

tion of synthetic fuels or chemical intermediates in petrochemical industries [2]. Particularly, combined steam and dry reforming of methane (CSDRM, 3CH₄ + 1CO₂ → 8H₂ + 4CO), also known as bireforming [3–6], appears as a very promising CO₂ valorization route yielding a syngas with H₂/CO molar ratio close to 2, called metgas [3–6]. The latter can be directly used in methanol [4–10] or dimethylether production [5–10] as well as in some Fisher-Tropsch operations aiming the preparation of long hydrocarbons chains [11,12]. By comparison, conventional dry reforming of methane (DRM, CH₄ + CO₂ → 2H₂ + 2CO) and steam reforming of methane (SRM, CH₄ + H₂O → 3H₂ + CO) yield a H₂/CO ratio of either 1 (too low) or around 3 (too high), respectively, which imposes supplementary stages (often expensive) if adjustment of the product ratio near 2 is required for the next steps of the process [3–6,13,14]. Moreover, from a sustainable point of view, the CSDRM reaction presents as additional benefit to consume CH₄, CO₂ and water as main reactants, these gases being also those present in biogas, a non-fossil fuel resource [3–6]. Thus, CSDRM offers a way to produce metgas from renewable energy sources without the need of auxiliary separation and purification procedures.

* Corresponding author at: CNRS UMR 7197, UPMC, Laboratoire de Réactivité de Surface, 4 place Jussieu, 75005 Paris, France.

** Corresponding author at: Department of Chemical Engineering, Faculty of Engineering, University of Balamand, P.O. Box 33, Amioun, El Koura, Lebanon.

E-mail addresses: pascale.massiani@upmc.fr (P. Massiani),

nissrine.hassan@balamand.edu.lb (N. El Hassan).

Compared to SRM and DRM, bibliographic reports on CSDRM are less numerous due to the highest complexity of this reaction that requires steam and high temperatures, as already discussed in our recent paper [15]. The main direction for catalyst development in this field is focused on the use of nickel as active phase. This transition metal is indeed the most attractive candidate for large-scale industrial applications due to its high reactivity in DRM and SRM [3–5] together with low cost and wide availability compared to noble metals (Ru, Rh, Ir) [16–19]. However, the stability of supported Ni-based catalysts under the harsh reaction conditions of CSDRM [20–23] is still an important concern. The major deactivation drawbacks are severe coke deposition, reoxidation and thermal agglomeration of the Ni⁰ nanoparticles under steam and at high temperature [24–39].

For SRM and DRM catalysts, it was recently found that confinement of the nickel active phase within structured pores of oxide supports, especially mesoporous silica [40–42] or alumina [43–46], helps minimizing Ni⁰ sintering during reaction, thus preserving reactivity with time on stream. Another effective approach to limit nanoparticles growth consists in forming a solid solution between impregnated nickel and the support by using appropriate synthesis techniques [3–5,24,25]. This is expected to stabilize the active phase by enhancing metal-support interaction (MSI) but also to limit coke formation associated to nickel sintering. Based on these approaches, we recently developed a mesoporous Ni-containing alumina catalyst obtained by combining (1) active phase introduction directly during the synthesis (“one-pot” synthesis allowing solid solution formation) and (2) use of an evaporation-induced self-assembly (EISA) method [47,48] in presence of a structuring agent (to obtain a mesoporous material). The resulting catalyst, with nickel nanoparticles highly dispersed and stabilized inside the structured alumina matrix, was found significantly more active and stable in long term CSDRM operation than impregnated catalysts [15].

Another general way to overcome deactivation relies on the introduction of secondary elements giving basic and/or redox properties to the catalyst. Table 1 summarizes available data dealing with this approach for CSDRM. Considering alumina-based materials with impregnated nickel, the most tested catalysts in this reaction, the presence of MgO [26,37,39], mixed CeO₂–ZrO₂ [38] or CeO₂ [28,34] was shown to inhibit deactivation whereas severe activity loss were seen in the absence of such added elements, with conversion levels dropping down by more than 50%, in some cases, after less than 20 h of reaction (Table 1). Similarly, mixed MgO–Al₂O₃ oxides derived from hydrotalcite like-materials were described as suitable supports leading to high CSDRM catalytic performances [37], even if some studies reported some deactivation on such type of systems and a need to add auxiliary elements to maintain stable performances [32,34–36]. Besides, catalysts with alumina-magnesia core-shells structures as supports were reported promising, demonstrating however a lack of selectivity towards metgas production [31]. It is commonly accepted that basic modifiers (e.g. MgO) in the catalyst formulation promotes CO₂ adsorption/activation on the surface and its subsequent reaction with neighbour carbon C_(s) deposits, leading globally to CO production (CO₂ + C_(s) → 2CO) [26,30,37]. Likewise, the addition of active oxygen carriers such as CeO₂ and/or ZrO₂ within Ni-based catalysts (Table 1) is known to result in oxidative removal of C_(s) deposits via their combustion with surface oxygen giving CO₂ [32,34,35]. However, most of the reported tactics that involve addition of a secondary element over “standard” commercial oxides require several successive time-consuming post-synthesis treatments, particularly (i) a step of high temperature calcination of the support prior to its utilization to generate mixed oxides (as in hydrotalcite like-materials [24,32–37] and in some cases in alumina [26–29,37]), (ii) subsequent calcination after Ni and/or co-element impregnation

[3–5,24–26,28–30,32–39] and (iii) eventually high temperature steam treatment (H₂/H₂O) following a H₂ reduction session [25].

Based on this state of the art, the present work aimed at combining the special advantages for CSDRM of (i) one-pot synthesized mesoporous nickel alumina catalysts with (ii) the promising behaviour expected by addition of a basic modifier. It is worth noting that, even if the benefits of ordered mesoporous oxide supports (particularly silica) is now well admitted for methane reforming reactions as was reviewed recently [49], the positive impact of structured mesoporous supports other than silica has not yet been established for CSDRM, except in our recent preliminary paper [15]. Thus, the goal was to develop “one-pot” mesoporous nickel alumina based catalysts containing a basic modifier for effective combined steam and dry reforming operation. As far as we know, such approach combining (i) structuration of the porous alumina support and (ii) active phase – and supplementary element – insertion within the catalyst matrix by “one-pot” synthesis was not yet considered for the CSDRM reaction (Table 1). Low cost and widely available Mg²⁺ and Ca²⁺ containing salts were chosen as additives based on their potentiality to yield basic properties (in their oxide form) and on their known positive impact on CSDRM (Table 1) and DRM [50–52]. For the sake of completion, the influences of the Ni content (5–10 wt% range) and of the nature and amount of the identified carbon species on the activity level and long-term stability were also considered.

2. Experimental procedures

2.1. Synthesis of mesoporous “one-pot” alumina based-materials

The mesoporous Ni_xAl₂O₃ (with x=5, 7.5 or 10 wt%) and Ni₅%M₅Al₂O₃ (where M=Mg or Ca) samples were synthesized following a procedure inspired (with some modifications) from the known “one-pot” evaporation-induced self-assembly (EISA) method [47,48]. For each synthesis, approximately 1.0 g of P123 Pluronic triblock copolymer ((EO)₂₀(PO)₇₀(EO)₂₀, M_n = 5800, Sigma Aldrich, 43546-5) was dissolved at room temperature (RT) in 20 mL of absolute ethanol (CH₃CH₂OH, Sigma Aldrich, 64-17-5) under vigorous stirring. Then, 1.6 mL nitric acid (65.0 wt% aqueous HNO₃, Johnson Matthey S.A., extra pure) was added, still under stirring, together with A mmol of aluminium isopropoxide (Al(OPr)₃, C₉H₂₁AlO₃, 98 + %, Sigma Aldrich, 220418), B mmol of nickel nitrate hexahydrate (Ni(NO₃)₂·6H₂O, Sigma Aldrich, 13478-007) and eventually C mmol of either magnesium nitrate hexahydrate or calcium nitrate tetrahydrate (Mg(NO₃)₂·6H₂O or Ca(NO₃)₂·4H₂O, Sigma Aldrich 13446-18-9 and 13477-34-4, respectively). All employed chemicals were used as received, without further purification. The total molar composition was always kept constant, equal to 10 mmol (i.e. [A+B] = 10 mmol for Ni_xAl₂O₃ samples and [A+B+C] = 10 mmol for Ni₅%M₅Al₂O₃ ones). The resulting mixture was covered with a polyethylene (PE) film, continuously stirred at RT for at least 7 h until complete dissolution and finally transferred into a beaker placed for 48 h in a digital auto-regulator water-bath (Stuart SWB6D) set at 60 °C to undergo slow evaporation (ethanol, acid). The obtained green xerogels, which color deepened with increasing Ni content (in line with increasing octahedral Ni²⁺ ions amounts), were calcined slowly in air at 600 °C for 5 h (heating rate 0.5 °C min⁻¹) to give calcined “one-pot” synthesized alumina-based materials.

2.2. Characterization techniques

Textural properties were determined from N₂-sorption (adsorption and desorption) isotherms recorded on an ASAP 2020 Micromeritics apparatus. Prior to experiments, the samples were

Table 1

Bibliographic listing of the different types of supported Ni-based catalysts and their performances in CSDRM.

Catalyst ^a	S.A. ^b	Ni	Co-metal	Rr ^c	T	GHSV	Initial performance			TOS ^d	deac. ^e	Final performance			Ref.
							(wt%)	(nature, wt%)	(°C)	(L _{cat} ⁻¹ h ⁻¹)	CH ₄ conversion (%)	CO ₂ conversion (%)	H ₂ /CO Molar ratio	(h)	CH ₄ conversion (%)
Ni/Al ₂ O ₃	107	12	–	1/0.4/0.8	750	530	71	n.m.	n.m.	20	C, S	64	n.m.	n.m.	[26]
Ni/MgO-Al ₂ O ₃	70	12	MgO, 20	1/0.4/0.8	750	530	76	n.m.	n.m.	20	C, S	75	n.m.	n.m.	[26]
Ni/Al ₂ O ₃	n.m.	12	–	1/0.4/0.8/1	800	265	81	n.m.	7	32	C	n.m.	n.m.	n.m.	[27]
Ni-CeO ₂ -ZrO ₂	97	15	Ce ₈₀ Zr ₂₀	1/0.4/0.8/1	800	265	97	80	1.9	20	–	95	78	n.m.	[27]
Ni/Al ₂ O ₃	3	12	–	1/0.4/0.8/1	700	530	62	40	n.m.	20	C, S	18	12	n.m.	[28]
Ni-Ce/Al ₂ O ₃	10	12	CeO ₂ , 6	1/0.4/0.8/1	700	530	72	57	n.m.	20	C, S	70	43	n.m.	[28]
Ni/Al ₂ O ₃	n.m.	4	–	1/0.3/0.7/3	750	60	89	49	1.49	14	n.m.	89	49	1.49	[29]
Ni/Rh/Al ₂ O ₃	n.m.	4	Rh, 0.04	1/0.3/0.7/3	750	60	89	44	1.63	14	n.m.	89	44	1.63	[29]
Ni/Al ₂ O ₃	n.m.	15	–	1/1/0.16	750	n.m.	95	90	0.9	n.m.	C, S	n.m.	n.m.	n.m.	[30]
Ni/MgO-Al ₂ O ₃	n.m.	15	MgO, 15	1/1/0.16	750	n.m.	100	92	1.1	n.m.	C, S	n.m.	n.m.	n.m.	[30]
Ni-Al ₂ O ₃	n.m.	10	–	1/0.3/0.7	800	30	92	76	2.70	50	C	92	75	2.70	[31]
Ni-MgO-Al ₂ O ₃	n.m.	10	MgO, 15	1/0.3/0.7	800	30	94	74	2.80	50	–	94	74	2.80	[31]
Ni/MgO-Al ₂ O ₃	n.m.	10	–	1/0.4/0.8/1	700	530	77	62	2.20	16	C	n.m.	n.m.	n.m.	[32]
Ni-Ce/MgO-Al ₂ O ₃ ^f	26	10	CeO ₂ , 2.5	1/0.4/0.8/1	700	530	81	66	2.1	16	–	n.m.	n.m.	n.m.	[32]
Ni/MgO-Al ₂ O ₃	108	12	MgO, 70	1/0.4/0.8/1	750	530	97	71	2.3	5	C, S	97	71	2	[33]
Ni/MgO-Al ₂ O ₃	112	12	MgO, 30	1/0.4/0.8/1	750	530	97	84	2	5	–	97	84	2	[33]
Ni/MgO-Al ₂ O ₃ ^f	118	12	–	1/0.4/1/1	850	n.m.	85 ^g	47 ^g	2.27 ^g	20	C, S	81 ^g	44 ^g	2.8 ^g	[34]
Ni-Ce/MgO-Al ₂ O ₃ ^f	117	12	CeO ₂ , 4	1/0.4/1/1	850	n.m.	86 ^g	58 ^g	2.15 ^g	20	–	83 ^g	52 ^g	2.2 ^g	[34]
Ni/MgO-Al ₂ O ₃ ^f	118	15	–	1/0.4/1/1	850	n.m.	74 ^g	35 ^g	2.22 ^g	20	C, S	77 ^g	32 ^g	2.19 ^g	[35]
Ni-Ce-Zr/MgO-Al ₂ O ₃ ^f	137	15	Ce ₈₀ Zr ₂₀ , 15	1/0.4/1/1	850	n.m.	81 ^g	44 ^g	2.29 ^g	20	–	81 ^g	41 ^g	2.24 ^g	[35]
Ni/MgO-Al ₂ O ₃ ^f	80	15	–	1/1/0.16	750	n.m.	95	90	n.m.	n.m.	C	n.m.	n.m.	n.m.	[36]
Ni-La/MgO-Al ₂ O ₃ ^f	81	15	La ₂ O ₃ , 10	1/1/0.16	750	n.m.	100	95	n.m.	n.m.	–	n.m.	n.m.	n.m.	[36]
Ni/MgO	6	12	–	–	–	–	60	n.m.	n.m.	20	C	56	n.m.	n.m.	[37]
Ni/Al ₂ O ₃	4	n.m.	–	–	–	–	72	n.m.	n.m.	5	C	35	n.m.	n.m.	[37]
Ni/CeO ₂	9	12	–	1/0.4/0.8	800	265	57	n.m.	n.m.	20	C	46	n.m.	n.m.	[37]
Ni/ZrO ₂	17	12	–	–	–	–	64	n.m.	n.m.	20	C	73	n.m.	n.m.	[38]
Ni/MgO-Al ₂ O ₃	108	12	MgO, 30	–	–	–	92	n.m.	n.m.	20	–	89	n.m.	n.m.	[38]
Ni/CeO ₂	9	15	–	1/0.4/0.8	800	265	58	n.m.	n.m.	20	C, S	47	n.m.	n.m.	[38]
Ni/ZrO ₂	17	15	–	–	–	–	78	n.m.	n.m.	20	C, S	63	n.m.	n.m.	[38]
Ni/CeO ₂ -ZrO ₂	60	15	Ce ₈₀ Zr ₂₀	–	–	–	94	n.m.	n.m.	20	C, S	82	n.m.	n.m.	[39]
Ni/SBA-15	n.m.	10	–	1/0.5/0.75	850	27	98	86	1.74	600	C, S, R	85	50	2.2	[39]
Ni/MgO-SBA-15	n.m.	10	MgO, 3	1/0.5/0.75	850	27	98	91	1.71	600	R	98	79	1.9	[39]

n.m. not mentioned.

^a Catalysts are identified based on the Ni deposition method: "Ni/" indicates post-impregnation of Ni (and of the secondary metal) on the support and "Ni–" indicates direct deposition of Ni (and of the secondary metal) in the course of synthesis.^b Surface area (S.A.) of the catalyst.^c Molar composition of feeding reactants (CH₄/CO₂/H₂O/diluent (Ar or N₂)- mol/mol/mol/mol).^d Time on stream (TOS) defined as the duration of stability measurements at a fixed temperature.^e Deactivation (Deac.) is classified in terms of: Coke deposition (C), sintering (S) and/or reoxidation (R) of metallic nanoparticles.^f MgO_(x)-Al₂O_{3(y)} support having a composition of x=30% and y=70%.^g Reaction conducted at P= 10 bar otherwise the operation pressure is 1 bar in the remaining tabulated studies.

degassed under vacuum for 3 h at 300 °C then cooled down back to room temperature before being placed at liquid nitrogen temperature for measurements. Single point pore volumes were determined from the adsorption isotherms at a relative pressure of 0.990. Brunauer–Emmett–Teller (BET) surface areas were calculated from BET equation for a relative pressure (P/P_0) range between 0.05 and 0.25. Pore size distributions were calculated using the Barrett–Joyner–Halenda (BJH) method applied to the adsorption branch of the isotherm. For spent catalysts, calcination in air at 450 °C/5 h (0.5 °C min⁻¹) was performed prior to N₂-sorption analysis to remove carbon deposits before analysis.

Structural properties were studied by powder X-ray Diffraction (XRD) at small and wide angles. The small-angle measurements were done from 2θ of 0.5° to 4.0° (time per step: 1 s) on a BRUKER type D8 ADVANCE diffractometer equipped with a Cu K α irradiation source ($\lambda = 1.5418$ nm) and operating at 40 kV and 30 mA. The wide-angles data were obtained on a PANalytical XPert³ diffractometer using a Cu K α radiation ($\lambda = 1.5405$ nm), a voltage of 30 kV, a current of 10 mA and a step size of 0.04° (with 2 s duration at each step). The acquisitions were done in a 2θ range from 20.0 to 90.0°. Crystalline phase identification was based on comparison with standard powder XRD files published by the international center for diffraction data (ICDD). Coherent domain sizes were calculated using the Scherrer's equation: $D_{(hkl)} = (K\lambda/\beta\cos\theta)$, where $K=0.9$ is the shape factor for spherical particles, λ is the X-ray wavelength, β is the full width at half maximum (FWHM) of the diffraction peak and θ is the peak position.

The reducibility of the Ni-alumina based materials was studied by temperature-programmed reduction (H₂-TPR) on an Autochem 2920 unit, Micromeritics. The calcined powder (100 mg) was loaded in a U-shaped quartz reactor and heated from RT up to 900 °C at a constant rate of 7 °C min⁻¹ under a 5 vol% H₂/Ar flow (30 mL min⁻¹). The overall H₂ consumption was constantly recorded by thermal conductivity detection (TCD). Before arrival to the detector, the gas flow was passed through a cold trap (composed of ice and NaCl) in order to condense any water generated during the experiment (NiO + H₂ → Ni⁰ + H₂O). This ensures that the detected signal (difference in thermal conductivity between reference and analysis gases) is fully related to H₂ consumption with no interference of formed water.

Transmission electron microscopy (TEM) observations were done on ultrathin sections of solids to correctly visualise the dispersed nickel nanoparticles (and eventual coke deposits) and their location inside or outside the porous alumina grains. The sections were prepared as follows: a few milligrams of powder were mixed with an EPON 812 embedding resin in a beam capsule. Polymerization of the mixture took place at 60 °C for 48 h, then the polymerized blocks were cut with a diamond knife in slices (50–70 nm in thickness) that were deposited on copper grids covered with a carbon membrane layer. TEM images were taken on a JEOL-JEM 200 electron microscope operating at 200 keV (LaB₆ gun). Average metallic Ni⁰ particle sizes were estimated using the "Comptage de Particules" LRS software considering at least 500 particles present in grains with main elongation axis (channels) orientated parallel to the electronic beam (i.e. pore openings perpendicular to the beam). Scanning electron microscopy (SEM) micrographs were registered on a Hitachi SU-70 SEM-FEG microscope with an electron acceleration tension of 7 kV.

TGA/DSC were performed on a TA SDT Q600 thermal analyzer instrument from RT to 900 °C (heating rate of 10 °C min⁻¹) in flowing air (50 mL min⁻¹). Raman spectra were collected on a KAISER (RXN1) optical system equipped with a charge-coupled detector (CCD), a laser with $\lambda = 785$ nm (energy of 1.58 eV) and a microscope with an X50 long working distance (W.D. = 8.0 mm) lens. The operation conditions were as follows: 10 mW laser power, 4 cm⁻¹

resolution, 10 s acquisition time and a total of 30 accumulations per spectrum.

2.3. Thermodynamic simulation of the CSDRM reaction

Simulations were performed using the HSC 7.1 Chemistry software (where H, S and C stand for the enthalpy, entropy and heat capacity, respectively) which principle is to calculate, based on the Gibbs free energy minimization's principle [53], the equilibrium gas composition depending on the applied conditions (initial molar gas mixture, temperature, pressure, etc.). For reasons detailed in Section 3.2, the chosen initial gaseous CH_{4(g)}/CO_{2(g)}/H₂O_(g)/Ar_(g) composition was 1/0.4/0.8/12 (Ar is used as inert diluent). C_(s) (carbon in solid phase) was introduced as possible product (initial composition set at zero). Equilibrium compositions (unconverted reactants and expected H_{2(g)}, CO_(g) and C_(s) products were determined in the 100–1000 °C temperature range.

2.4. Reactivity measurements

Catalytic tests were conducted at atmospheric pressure (P = 1 atm) in a Microactivity (PID Eng and Tech) vertical fixed-bed continuous flow stainless steel (SS310) reactor (9 mm internal diameter). Prior to reaction, the calcined powder was *in-situ* reduced at 800 °C/3 h under a flow (30 mL min⁻¹) of 5 vol% H₂/Ar in order to ensure complete nickel reduction, then the flow was switched to the reactant mixture (CH₄/CO₂/H₂O/Ar = 1/0.4/0.8/12). Water was introduced by a syringe pump (Teledyne ISCO, D-series, model 5000) in the form of liquid water (0.005 mL min⁻¹), evaporated (6.15 mL min⁻¹) at 180 °C (hotbox temperature) and mixed with the other gases before feeding the reactor. The total gas hourly space velocity (GHSV) was 69 L g_{cat}⁻¹ hr⁻¹ or 138 L g_{cat}⁻¹ hr⁻¹ (using 100 and 50 mg catalyst weight, respectively). The reaction temperature was controlled by a thermocouple placed in the middle of the catalyst bed. The effect of temperature (600–800 °C range) on CH₄ and CO₂ conversions upon either increase or decrease of the temperature was evaluated along successive 3 h stabilization steps at each temperature. Long-term stability measurements were carried out at 800 °C for 40 h.

Before analysis, the effluent was passed through a gas/liquid separator to condense the residual steam present in the exhaust gas after reaction. Next, the reactants and products were quantified by on-line gas chromatography using a Micro-GC Inficon equipped with a thermal conductivity detector (TCD) and two columns placed in parallel for the detection of CH₄, H₂ and CO (Molecular Sieve column) and of CO₂ (plot U column). The results will be hereafter expressed as conversion of CH₄ (XCH₄), conversion of CO₂ (XCO₂), and H₂/CO ratio calculated according to Eqs. (1)–(3):

$$X_{\text{CH}_4} (\%) = \frac{[\text{CH}_4]_{\text{in}} - [\text{CH}_4]_{\text{out}}}{[\text{CH}_4]_{\text{in}}} \times 100 \quad (1)$$

$$X_{\text{CO}_2} (\%) = \frac{[\text{CO}_2]_{\text{in}} - [\text{CO}_2]_{\text{out}}}{[\text{CO}_2]_{\text{in}}} \times 100 \quad (2)$$

$$\frac{\text{H}_2}{\text{CO}} = \frac{\text{mol of H}_2 \text{ produced}}{\text{mol of CO produced}} \quad (3)$$

3. Results and discussion

3.1. Textural and structural properties of calcined samples

The textural and structural properties of calcined materials were analysed by N₂ sorption and by small and wide angles XRD measurements. The N₂ sorption isotherms (Fig. 1A) are of type IV for all samples, with H₁-shaped hysteresis loops and steep capillary condensation steps at $P/P_0 = 0.6$ –0.8 typical of ordered mesoporous

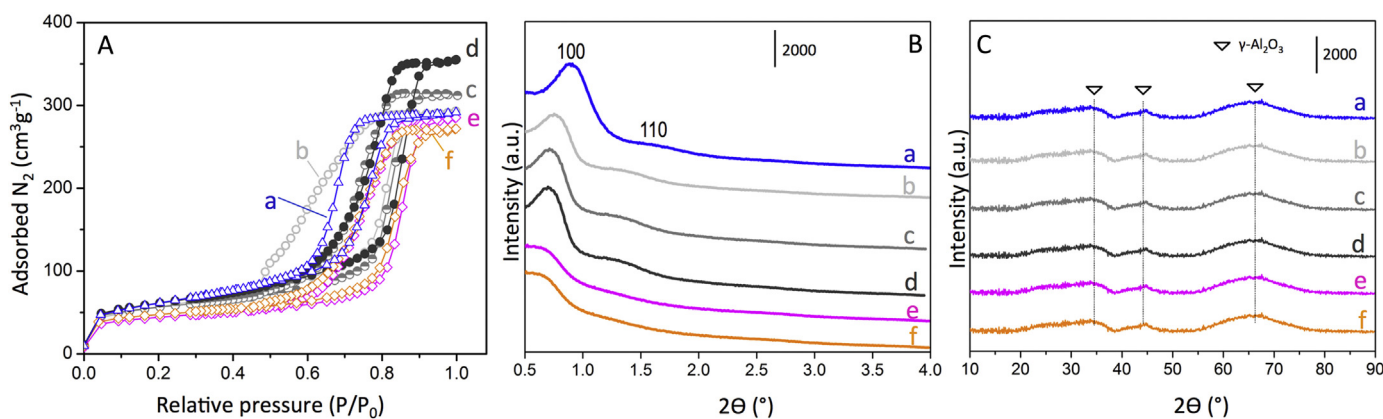


Fig. 1. (A) N₂ adsorption-desorption isotherms and (B) low and (C) wide angles XRD patterns of calcined samples: (a) Al₂O₃, (b) Ni_{5%}Al₂O₃, (c) Ni_{7.5%}Al₂O₃, (d) Ni_{10%}Al₂O₃, (e) Ni_{5%}Ca_{5%}Al₂O₃ and (f) Ni_{5%}Mg_{5%}Al₂O₃. For XRD patterns, an offset was applied along Y-axis for the sake of clarity.

structures with parallel and cylindrical channels [47,54]. The desorption branch for Ni_{5%}Al₂O₃ (curve b, Fig. 1A) is slightly different than for other samples, with a shape characteristic of “ink-bottle” interconnected pores having different size distributions of cavities and necks [55]. This could be due to some experimental uncertainty during preparation of this sample that was the first synthesized according to our experimental procedure (not yet optimized). In spite of such small difference, the well-ordered 2D hexagonal structure (p6 mm symmetry) is also attested in all synthesised materials by the low angle X-ray diffraction patterns (Fig. 1B) that show two peaks at circa 0.94° and 1.5° (even if very weak for both doped materials), characteristic of the [1 0 0] and [1 1 0] plane reflections, respectively [47].

The good textural properties of all samples can also be seen from the values of surface area, pore volumes and pore diameters deduced from the isotherms (Table 2). Particularly, in all the Ni_xAl₂O₃ series, the surface areas are in the range 200–225 m² g⁻¹, as high as in previous reports on mesoporous alumina synthesized under comparable conditions [47]. For all samples (except Ni_{5%}Al₂O₃ with “poorly-controlled” texture), the pores sizes distributions are quite sharp (diameter between 8 and 12 nm), within the conventional range for mesoporous materials. At higher Ni content, the adsorption branch of the hysteresis loop gradually shifts to higher relative pressures, revealing larger pores, and the phenomenon is slightly accentuated for the Mg and Ca containing samples. Again, this trend is in accordance with the shifts towards lower angles seen in the small angles XRD patterns (Fig. 1B). This increase could be related to the nitrate ions added in the medium during synthesis (present as counter ions in the Ni, Mg and Ca pre-

cursors), which could acidify the ethanol solution with subsequent enlargement of pore diameters as was already proposed [54]. Such pH effect, together with possible access restriction to some pores by occluded species, could also contribute to the slight loss of surface area and pore volume seen in Ni_{5%}Al₂O₃ compared to Ni-free Al₂O₃, and accentuated in Ni_{5%}Mg_{5%}Al₂O₃ and Ni_{5%}Ca_{5%}Al₂O₃. It is worth recalling here that such textural changes cannot derive from the activation procedure since all samples underwent the exact same thermal treatments. Besides, the main notable evolution in the Ni_xAl₂O₃ series is the increase of pore volume with Ni enrichment, as already reported on analogous “one-pot” synthesized Ni-alumina materials calcined at 400 °C, but not yet clarified [47].

With respect to high angles XRD measurements, all calcined materials exhibit a comparable pattern (Fig. 1C), independently on the Ni (and eventually Mg or Ca) content. Thus, only weak broad diffraction peaks characteristic of a γ-Al₂O₃ phase (ICDD file # 10-0425) with small crystalline domains are observed, and no peak attributable to nickel crystalline phases is seen in the Ni loaded samples, revealing an amorphous character or an extremely high dispersion of nickel expected to be present in all samples.

Confirmation that nickel species were indeed present in all Ni-enriched materials was obtained from TPR profiles of calcined nickel loaded samples that systematically showed a main reduction peak at rather high temperature (550–800 °C, curves b-f, Fig. 2A). Such type of profile, already reported for “one-pot” synthesized Ni-alumina materials [44], is typical of the reduction of oxidized Ni strongly interacting with the support, as in spinel mixed phases characterized by strong MSI [56]. Remarkably, no

Table 2
Textural properties of calcined samples and H₂-uptakes during reduction.

Sample	Ni and additive content (wt%)	N ₂ -sorption analysis						H ₂ -uptakes	
		BET specific surface area (m ² g ⁻¹)		Pore volume (cm ³ g ⁻¹)		Average pore diameter (nm) ^b		Total H ₂ -uptake (μmol g ⁻¹) ^c	Exp.
		calc. ^a	red. ^a	calc. ^a	red. ^a	calc. ^a	red. ^a		
Al ₂ O ₃	–	225	142	0.46	0.35	8±4	8±6	25	–
Ni _{5%} Al ₂ O ₃	5.0 Ni	215	111	0.45	0.33	9±5	9±5	941	900
Ni _{7.5%} Al ₂ O ₃	7.5 Ni	208	139	0.49	0.39	10±6	10±6	1339	1350
Ni _{10%} Al ₂ O ₃	10.0 Ni	201	180,101 ^d	0.55	0.45,0.28 ^d	11±6	11,13 ^d ±6	1761	1800
Ni _{5%} Ca _{5%} Al ₂ O ₃	5.0 Ni,5.0 Ca	157	105	0.42	0.36	12±5	11±5	945	900
Ni _{5%} Mg _{5%} Al ₂ O ₃	5.0 Ni,5.0 Mg	169	115	0.44	0.40	12±6	12±5	928	900

^a Textural values after (calc.) calcination at 600 °C for 5 h and (red.) subsequent H₂-reduction at 800 °C for 3 h.

^b Average pore diameter ± standard deviation from the maxima.

^c H₂-uptakes (Exp.) determined experimentally from TPR profiles after complete reduction at T=900 °C and (The) theoretical values calculated from the expected Ni²⁺ content.

^d Textural values obtained over the spent catalyst after re-calcination (450 °C/5 h) for removal of carbon deposits.

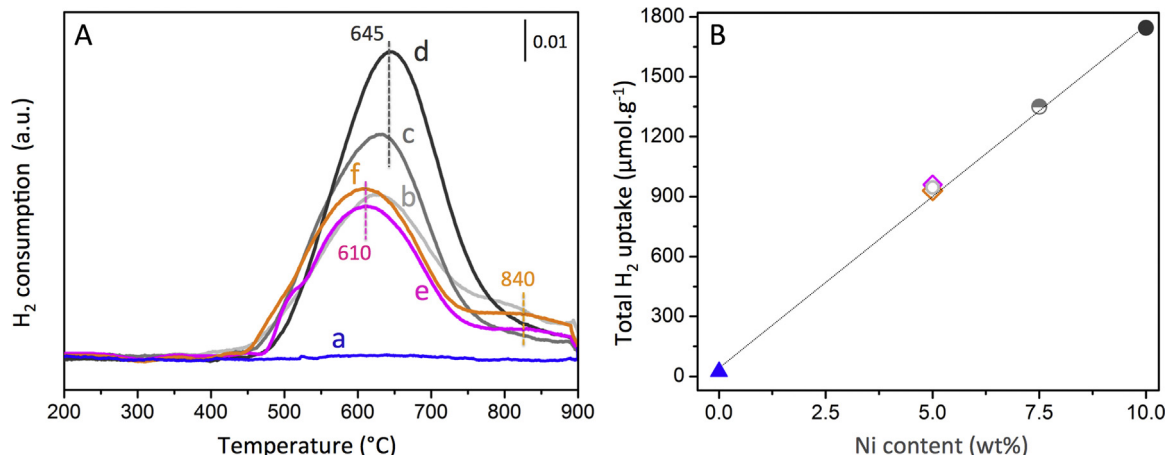


Fig. 2. (A) H₂-TPR profiles and (B) total experimental H₂-uptake as a function of Ni content (wt%) for calcined alumina based samples: (a) Al₂O₃, (b) Ni_{5%}Al₂O₃, (c) Ni_{7.5%}Al₂O₃, (d) Ni_{10%}Al₂O₃, (e) Ni_{5%}Ca_{5%}Al₂O₃ and (f) Ni_{5%}Mg_{5%}Al₂O₃.

peak of weakly bounded Ni species (reduction temperature below 500 °C) such as those identified on non-porous impregnated alumina samples [15,43,56] was detected, revealing strong support metal interaction for all introduced nickel. For both Ni_{5%}Mg_{5%}Al₂O₃ and Ni_{5%}Ca_{5%}Al₂O₃ materials, a peak at very high temperature (above 800 °C) is also seen (profiles e and f, Fig. 2A), although very weak, possibly indicative of Ni in even stronger interaction and/or of some reduction of Mg or Ca derived species. As expected, no reduction peak was detected over pure alumina (profile a, Fig. 2A). Experimental H₂-uptakes (200–900 °C range) estimated from above profiles are compared in Table 2 to theoretical uptakes calculated by (i) considering the expected Ni content in each nickel-loaded sample and (ii) assuming a bivalent nickel oxidation state after calcination. The excellent agreement between values is also attested by the linear correlation between H₂-uptakes and Ni contents (Fig. 2B). This proportionality confirms that all nickel introduced in the solution during synthesis (i) is recovered in the solid after preparation, (ii) is present at a divalent state in the calcined materials and (iii) is fully reducible below 900 °C. Combined with the close peak positions for all samples, this stresses out the similar nature of the Ni species, independently of the material composition. Moreover, it is worth recalling that these species were not detected in X-ray diffraction patterns (see above), revealing an amorphous state and/or a high dispersion of nickel oxide nanospecies having crystalline domains with sizes below the XRD detection limit. Small shifts in the position of the main peak are nevertheless noted between samples. In the Ni_{x%}Al₂O₃ series (profiles b–d, Fig. 2A), the temperature of the maximum of the peak increases from 626 °C to 631 °C then 645 °C when passing from 5 to 7.5 then 10 wt% Ni. Recalling that TPR is carried out in dynamic conditions, such trend could simply result from the different nickel contents, higher amounts of reducible species shifting the maximum of the process towards higher temperatures. Differences in Ni-based particles sizes could also play a role, but this is not probable here in view of the close Ni dispersion in all samples discussed below (Section 3.6). Contrarily, for both Ni_{5%}Mg_{5%}Al₂O₃ and Ni_{5%}Ca_{5%}Al₂O₃ samples, the peak slightly shifts towards lower temperatures (peak maxima around 610 °C, profiles e–f, Fig. 2A) compared to Ni_{5%}Al₂O₃ with same Ni content (peak maximum around 630 °C, profile b, Fig. 2A), suggesting some weakening of the nickel-support interaction when Mg or Ca are present. A similar observation was previously attributed to a potential competition between nickel and calcium/magnesium in the interaction with the alumina substrate [57]. Also, an effect of the overall acidic-basic properties with changes of the chemical composition could be involved.

The textural features of the samples were also examined after reduction (800 °C, 3 h). Compared to their calcined forms, the reduced materials showed slightly smaller specific surface areas and reduced pore volumes (Table 2) indicative of some thermal contraction of the alumina framework and/or pore surface condensation by dehydration and/or dehydroxylation during the high temperature reduction treatment [58]. The values remain however fully satisfying for mesoporous materials treated at such temperature, revealing a high thermal resistance.

3.2. Thermodynamics aspects and choice of catalytic conditions

Before CSDRM testing, the best conditions to use for conducting the reaction were checked from thermodynamic simulations. Equilibrium values at atmospheric pressure (as used in the experiments) were thus determined for the applied gaseous composition, taking into account possible formation of a carbon solid phase (representing carbon deposition that cannot be ignored during practical reforming conditions). From the obtained gases concentrations plotted as a function of temperature between 100 and 1000 °C (Fig. 3A), CSDRM can be viewed as a multi-reactions network where various reactions occur simultaneously, at levels that depend on the operating temperature. The possible reactions (i.e. main CSDRM that combines SRM and DRM, and side reactions [59]) as well as their favourable temperature zones are specified in Table 3.

Both steam and dry methane reforming (and therefore CSDRM as well) predominantly take place above 600 °C but with co-existence of some side reactions until 750 °C (particularly methane decomposition, WGS and RWGS, Table 3). This yields, in the 600–750 °C temperature range (Fig. 3B), to H₂:CO molar products ratios far above the desired value of about 2, and to “apparent” very low CO₂ conversions due to high occurrence of water gas shift reaction producing CO₂, the latter being then not only a reactant but also a product of reaction. Effective combination of both SRM and DRM (i.e. CSDRM) to produce metgas is therefore not possible unless operating above 750 °C (upper zone 3 and zone 4 in Table 3).

Besides, although the C_(s) profile shows significant decrease of carbon formation above 750 °C (Fig. 3A), CH₄ decomposition still remains one possible reaction route at such high temperatures. This can ultimately cause severe catalytic deactivation in case of graphitic carbon deposition (even in low amount) as often observed with Ni-based methane reforming catalysts (including CSDRM ones, Table 1). A recognized solution to overcome this drawback while keeping a good control of the final product ratio close to 2 consists in adding some excess H₂O and CO₂ in the

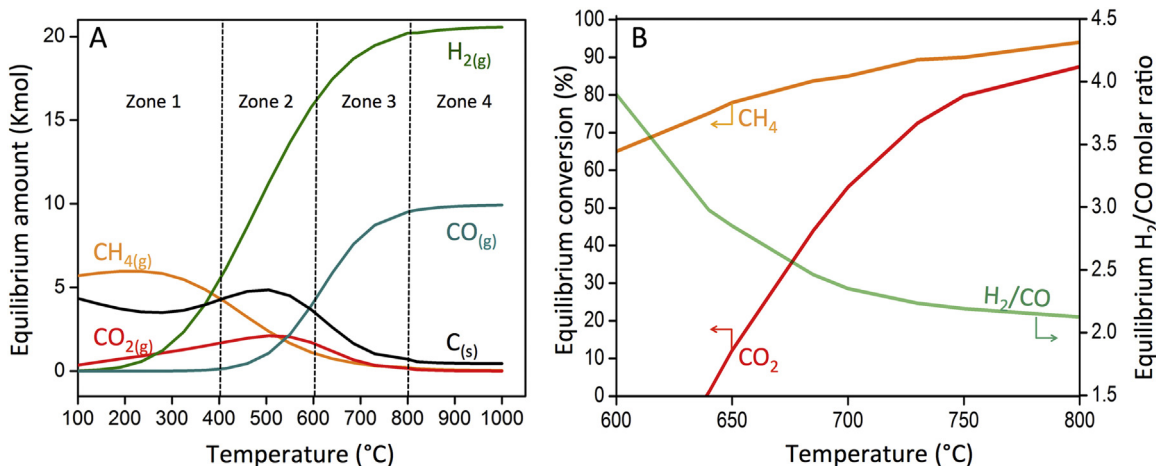


Fig. 3. (A) Thermodynamic equilibrium plots (100–1000 °C) and (B) related equilibrium conversions (CH_4 and CO_2) and molar product H_2/CO ratios (600–800 °C) under CSDRM conditions; evaluations obtained from the HSC 7.1 chemistry software considering initial molar composition $\text{CH}_4/\text{CO}_2/\text{H}_2\text{O}/\text{Ar} = 1/0.4/0.8/12$ and including carbon $\text{C}_{(\text{s})}$ formation.

Table 3

List of main and side-reactions [59] possibly occurring during combined steam and dry reforming of methane and probability of occurrence (Favorable or Not Favorable) as evaluated from thermodynamic calculations of the Gibbs free energy change (ΔG) using the HSC 7.1 Chemistry software.

Reactions	Equations	Temperature range (°C)			
		100–400 Zone 1*	400–600 Zone 2*	600–800 Zone 3*	800–1000 Zone 4*
Reforming reactions					
Steam reforming of methane (SRM)	$\text{CH}_4 + \text{H}_2\text{O} \rightarrow 3\text{H}_2 + \text{CO}$	N.F.-F.	F.	F.	F.
Dry reforming of methane (DRM)	$\text{CH}_4 + \text{CO}_2 \rightarrow 2\text{H}_2 + 2\text{CO}$	N.F.	N.F. – F.	F.	F.
Combined steam and dry reforming of methane (CSDRM)	$\text{CH}_4 + 1/3\text{CO}_2 + 2/3\text{H}_2\text{O} \rightarrow 8\text{H}_2 + 4\text{CO}$	N.F.	N.F.	N.F.-F.	F.
Side reactions (non-coke forming)					
Water gas shift (WGS)	$\text{CO} + \text{H}_2\text{O} \rightarrow \text{CO}_2 + \text{H}_2$	F.	F.	F.-N.F.	N.F.
Reverse water gas shift (RWGS)	$\text{CO}_2 + \text{H}_2 \rightarrow \text{CO} + \text{H}_2\text{O}$	N.F.	N.F.-F.	F.	F.-N.F.
CO_2 methanation	$\text{CO}_2 + 4\text{H}_2 \rightarrow \text{CH}_4 + 2\text{H}_2\text{O}$	F.	F.-N.F.	N.F.	N.F.
Side reactions (coke forming)					
CO_2 hydrogenation	$\text{CO}_2 + 2\text{H}_2 \rightarrow 2\text{H}_2\text{O} + \text{C}_{(\text{s})}$	F.	F.-N.F.	N.F.	N.F.
CH_4 decomposition	$\text{CH}_4 \rightarrow 2\text{H}_2 + \text{C}_{(\text{s})}$	N.F.	N.F.-F.	F.	F.-N.F.
CO disproportionation (Boudouard)	$2\text{CO} \rightarrow \text{CO}_2 + \text{C}_{(\text{s})}$	F.	F.	F.-N.F.	N.F.
CO dehydrogenation	$\text{CO} + \text{H}_2 \rightarrow \text{H}_2\text{O} + \text{C}_{(\text{s})}$	F.	F.-N.F.	N.F.	N.F.
Selectivity (H_2/CO molar ratio)					
		344–37.1	37.1–3.9	3.9–2.1	2.1–2.0

*: Temperature zones as identified on Fig. 3A.

F.: favored reaction.

N.F.: not favored reaction.

N.F.-F. (or F.-N.F.): from not favored to favored (or reverse) on the considered zone.

gas feed ($\text{CH}_4/\text{CO}_2/\text{H}_2\text{O} = 1/0.4/0.8$ instead of $1/0.33/0.66$ theoretically expected for pure CSDRM) [3,4,26,28,37]. This composition and a temperature of 800 °C were consequently selected as operating conditions, being consistent with those currently applied for CSDRM (Table 1). For the sake of completion, the effect of temperature on activity levels was also analysed through measurements carried out between 600 and 800 °C upon either temperature increase or decrease.

3.3. Catalytic performances of alumina-based catalysts

Prior to catalytic runs, the calcined mesoporous materials were *in-situ* reduced till 800 °C to generate the Ni^0 metal state active in methane reforming. The flow was then switched to that of reactants (GHSV of $138 \text{ Lg}_{\text{cat}}^{-1} \text{ h}^{-1}$) and the catalytic measurements were performed upon stepwise temperature decrease down to 600 °C. The obtained conversion values (X_{CH_4} , X_{CO_2}) and product ratios (H_2/CO) are listed in Table 4 and plotted as a function of temperature in Fig. 4 (where the X-axis scale follows the decreasing temperature order applied during the experiments).

As expected from the endothermic character of the CSDRM reaction, both CH_4 and CO_2 conversions declined with temperature decrease and the effect was more pronounced for CO_2 , particularly at temperatures below 700 °C (Fig. 4B). This is in accordance with the interference of WGS side-reaction discussed above (Section 3.2). As also anticipated, an amelioration of the CH_4 and CO_2 conversions (curves a–c, Figs. 4A,B) was seen upon increase of the Ni content from 5 to 10 wt%, till reaching activity levels close to the maximum ones imposed by thermodynamics (dashed-lines).

More interestingly, addition of 5 wt% Mg (or Ca) was beneficial to both CH_4 and CO_2 conversions (curves d and e, Figs. 4A,B) compared to the catalyst with same 5 wt% Ni content but without additive (curve a, Figs. 4A,B), and the reactivity then even exceeded that of $\text{Ni}_{7.5}\text{Al}_2\text{O}_3$ (curve b, Figs. 4A,B) in spite of a lower nickel content. The reason of such enhanced activity in presence of either Mg or Ca, already reported in the literature [60–62], will be discussed in Section 3.7.

Complementary experiments involving again temperature variations were done by decreasing the temperature down to 600 °C after the *in-situ* H_2 -activation step (carried at 800 °C as above), then switching the gaseous feed to flowing reac-

Table 4Effect of reaction temperature on catalytic performance in combined steam and dry reforming of methane ($\text{CH}_4/\text{CO}_2/\text{H}_2\text{O} = 1/0.4/0.8/12$, $P = 1 \text{ atm}$, $\text{GHSV} = 69 \text{ L g}_{\text{cat}}^{-1} \text{ h}^{-1}$).

Samples	T = 600 °C				T = 700 °C				T = 800 °C			
	Conversion (%)		Conversion (%)		Conversion (%)		Conversion (%)		Conversion (%)		Conversion (%)	
	XCH ₄	XCO ₂										
Ni _{5%} Al ₂ O ₃	37	24	–	45	43	22	15	57	54	51	43	43
Ni _{7.5%} Al ₂ O ₃	44	35	–	55	49	29	24	66	60	61	50	50
Ni _{10%} Al ₂ O ₃	64	60	–	78	71	56	49	82	80	80	76	76
Ni _{5%} Ca _{5%} Al ₂ O ₃	45	35	–	60	54	53	44	69	65	61	57	57
Ni _{5%} Mg _{5%} Al ₂ O ₃	58	54	–	70	66	40	34	77	73	72	70	70

Samples	T = 600 °C				T = 700 °C				T = 800 °C			
	H ₂ /CO (molar ratio)***		H ₂ /CO (molar ratio)***		H ₂ /CO (molar ratio)***		H ₂ /CO (molar ratio)***		H ₂ /CO (molar ratio)***		H ₂ /CO (molar ratio)***	
	*	**	*	**	*	**	*	**	*	**	*	**
Ni _{5%} Al ₂ O ₃	4.3	4.3	2.6	2.9	2.2	2.4						
Ni _{7.5%} Al ₂ O ₃	4.1	4.2	2.7	2.7	2.2	2.3						
Ni _{10%} Al ₂ O ₃	4.1	4.2	2.4	2.5	2.3	2.4						
Ni _{5%} Ca _{5%} Al ₂ O ₃	4.2	4.2	2.5	2.6	2.1	2.2						
Ni _{5%} Mg _{5%} Al ₂ O ₃	4.1	4.1	2.6	2.6	2.1	2.1						

Average values calculated over 3 h step at each temperature passing from 800 down to 600 °C (*) or from 600 up to 800 °C (**) after *in-situ* H₂-reduction (800 °C/3 h).***: the precision of the H₂/CO molar ratio value is at ± 0.05 .

tants and conducting the measurements upon stepwise heating up to 800 °C (in place of stepwise decrease as done before). The thus obtained new activity levels led to a classification of catalysts as above ($\text{Ni}_{10\%}\text{Al}_2\text{O}_3 > \text{Ni}_5\text{Mg}_5\text{Al}_2\text{O}_3 > \text{Ni}_5\text{Ca}_5\text{Al}_2\text{O}_3 > \text{Ni}_{7.5\%}\text{Al}_2\text{O}_3 > \text{Ni}_5\text{Al}_2\text{O}_3$) but the conversions at a given temperature were systematically lower in the second set of experiments (Table 4). Moreover, at each temperature, the recorded H₂:CO molar ratio significantly deviated from the expected thermodynamic value, suggesting higher occurrence of side reactions. Both phenomena, indicative of lower catalytic performances, demonstrate that starting the catalytic run under stream at 800 °C (in place of 600 °C) is a more efficient stabilization procedure. A reason of the lowest reactivity attained after starting the catalysts testing at 600 °C could be the enhanced C_(s) deposition (Fig. 3A) occurring at this temperature (Table 3), leading to irreversible poisoning and/or access restriction to some active sites that become less numerous even upon subsequent heating at higher temperatures.

3.4. Long-term catalytic stability and selectivity to metgas

Long-term stability tests, a critical issue for catalyst development, were carried out at 800 °C for 40 h under reactant stream, directly after *in-situ* H₂-reduction (best conditions, as discussed above). The space velocity was kept at 138 L g_{cat}⁻¹ h⁻¹ (as above) because such condition was found appropriate for operating the reaction far enough from thermodynamic limitations at 800 °C (see Figs. 4A,B), which is requested to allow comparisons of activity levels between catalysts. On the contrary, the experiments carried out at a lower space velocity (69 L g_{cat}⁻¹ h⁻¹) led to conversions only few% below thermodynamic equilibrium (Table 5), due to the high performances of the present samples, being therefore hardly exploitable for comparisons purpose.

For all catalysts, the CH₄ conversions (Figs. 5A,A'), CO₂ conversions (Figs. 5B,B') and H₂:CO molar ratios (Figs. 5C,C') were found extremely stable with time-on-stream. In the Ni_{x%}Al₂O₃ series, the reactivity order was as above (Figs. 5A,B), following the Ni content order even if being not proportional to it. This may indicate diffusional limitations or, most probably, a number of active sites not proportional to the metal amount, suggesting in turn either a higher accessibility hindrance to the active Ni⁰ nanoparticles with nickel enrichment or a decrease of metal dispersion.

With respect to Mg and Ca additives, their beneficial effect towards conversions is still observed, even if less pronounced with Ca than with Mg (Fig. 5A',B'). Owing to the stable activity levels, it can also be seen that the CO₂ conversion is slightly lower than that of CH₄, on both catalysts, in accordance with the excess CO₂ in the gas feed (see Section 3.2) and with the thermodynamic values that estimate the CO₂ conversion lower by almost 6% than that of CH₄ at 800 °C (Fig. 3B). Moreover, the H₂:CO molar ratio obtained on these materials is close to 2 all along the 40 h of test (Fig. 5C'), demonstrating the absence (or very limited occurrence) of side reactions on these catalysts. By contrast, the H₂:CO molar ratio progressively deviates away from 2 with Ni enrichment in the Ni_{x%}Al₂O₃ series (Fig. 5C and Table 5) and the CH₄ conversion simultaneously approaches that of CO₂ (Table 5). In view of the H₂:CO ratio significantly above 2 for the two Ni-richest samples, methane cracking that can occur at 800 °C and that produces C_(s) and H₂ (Table 3) appears as the most probable side reaction taking place on these catalysts. This reaction consumes CH₄ and takes place over metal Ni⁰ nanoparticles where it can produce carbon deposits, possibly blocking the active sites and lowering methane conversion [14]. The reason why CO₂ is not simultaneously affected could be linked to the high surface area of the alumina based-catalysts containing slightly basic sites where CO₂ adsorption (then activation) could continue. For the sake of completion, it has to be recalled that RWGS that consumes CO₂ and produces CO is also possible at high temperature (Table 3), but its occurrence seems less probable since it would lead to a decrease (rather than increase) of the H₂:CO ratio.

Therefore, in addition to high activity levels, especially when doped with Mg or Ca additive, our “one-pot” synthesized mesoporous catalysts show excellent catalytic stabilities along high temperature CSDRM operation, at least as high or even better than those described in the few existing reports on CSDRM alumina-based catalysts (Table 1). By comparison, even if addition of MgO (5–20 wt%) on impregnated Ni/Al₂O₃ [26] or mesoporous Ni/SBA-15-based samples [39] was already found beneficial when conducting the same reaction at 750 °C–850 °C, the amelioration remained more limited. Also, high and stable CH₄ and CO₂ conversions were reported over core-shells Ni@Al₂O₃ and Ni@MgO-Al₂O₃ catalysts, but the selectivity to metgas was low (H₂:CO ratio as high as 2.70), even on a hydrotalcite like MgO containing sample used in conditions favorable to metgas production [31]. Besides, CSDRM

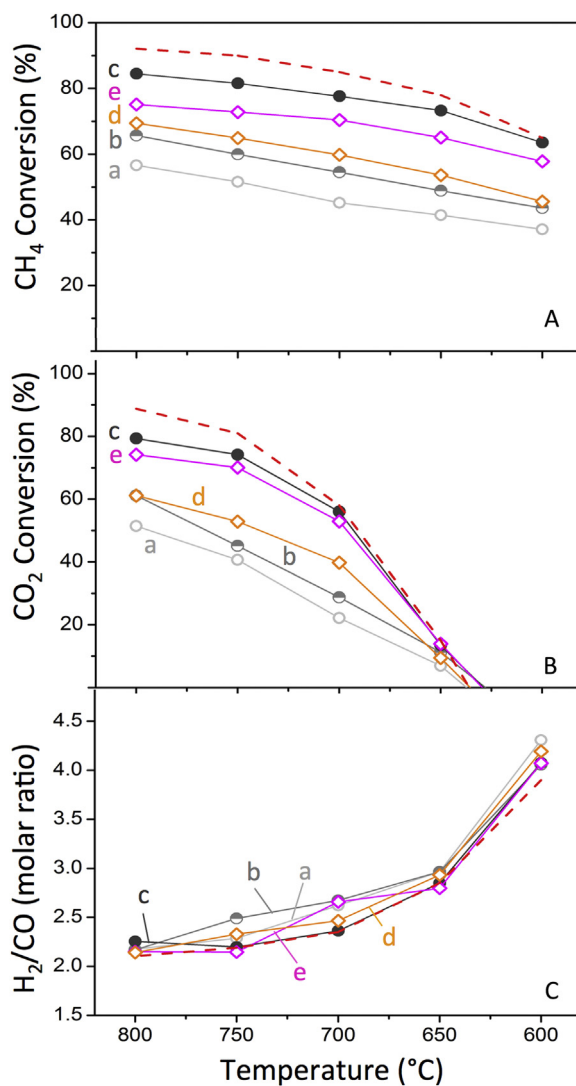


Fig. 4. Evolutions of (A) CH_4 conversion, (B) CO_2 conversion and (C) H_2/CO molar product ratio upon stepwise decrease of temperature from 800 to 600 °C during combined steam and dry reforming of methane ($P = 1 \text{ atm}$, $\text{GHSV} = 138 \text{ L g}_{\text{cat}}^{-1} \text{ h}^{-1}$) over *in-situ* reduced (a) $\text{Ni}_5\%\text{Al}_2\text{O}_3$, (b) $\text{Ni}_{7.5}\%\text{Al}_2\text{O}_3$, (c) $\text{Ni}_{10}\%\text{Al}_2\text{O}_3$, (d) $\text{Ni}_5\%\text{Ca}_5\%\text{Al}_2\text{O}_3$ and (e) $\text{Ni}_5\%\text{Mg}_5\%\text{Al}_2\text{O}_3$. The thermodynamic values (dashed-lines) were calculated with the HSC 7.1 Chemistry software.

performances as good as ours were attained on impregnated $\text{Ni}_{7.5}\%\text{Al}_2\text{O}_3$ [25] and $\text{Ni}_{12}\%\text{MgO-Al}_2\text{O}_3$ [24] catalysts featuring solid solution characteristics, but the preparation routes were quite complex with successive energy consuming (high temperature) and time-consuming (several steps) pre- and post-synthesis catalyst treatments.

3.5. Quantity and nature of coke after long term high temperature catalytic testing

To further understand the reasons of the good CDSRM performances of our samples, the spent catalysts (after stability run at 800 °C/40 h) were characterized by several techniques able to inform on coke deposits and on nickel dispersion and location. Combined TGA and DSC was carried out in flowing air, between 300 °C and 900 °C, to quantify carbon contents in the spent materials and identify the type of involved $\text{C}_{(s)}$ species from the temperatures at which they are oxidized (particularly sp^2 (grapheme, nanotubes) and sp^3 (graphite) carbon types) [63,64]. For all spent catalysts, the TGA profiles consisted of a main weight loss over a large temperature range (Fig. 6A, Table 5), fully attributable to carbon removal (as checked by on line mass spectrometry), and the DSC profiles showed three distinct peaks (Fig. 6B).

The first remarkable information provided by these data is the drastic decrease of the overall $\text{C}_{(s)}$ contents (Table 5) when comparing the spent $\text{Ni}_x\%\text{Al}_2\text{O}_3$ catalysts (between 9 and 19 wt% carbon) and the spent Mg- or Ca- modified ones (below 4 wt% carbon). This is in accordance with the above-mentioned methane decomposition occurring as side reaction on the former samples but not on the latter (Section 3.4). Secondly, in the spent $\text{Ni}_x\%\text{Al}_2\text{O}_3$ series, the coke content increases with Ni content, and it consequently follows activity levels as well. This is better illustrated on Fig. 7 that shows on a same graph the levels of methane conversions (average values from stability tests) and the coke contents for all catalysts. Such a correlation was in fact predictable since samples with more numerous active sites (higher Ni content) converting a higher quantity of reactants (higher conversions) should produce more carbon-based species (higher C content). Nevertheless, this trend no longer stands with the $\text{Ni}_5\%\text{Mg}_5\%\text{Al}_2\text{O}_3$ and $\text{Ni}_5\%\text{Ca}_5\%\text{Al}_2\text{O}_3$ catalysts that generate high reactivity levels but very low carbon amounts (Fig. 7), stressing again the peculiarly high resistance to coking of the Mg (or Ca) enriched materials. It is also worth noting that the stability tests performed on the $\text{Ni}_x\%\text{Al}_2\text{O}_3$ series of catalysts at $69 \text{ L g}_{\text{cat}}^{-1} \text{ h}^{-1}$ in place of $138 \text{ L g}_{\text{cat}}^{-1} \text{ h}^{-1}$, produced less coking (Table 5) contrarily to what is expected from higher contact time giving a priori higher conversion levels (Table 5). Nevertheless, in such experimental conditions, the activity levels approached thermodynamic limits due

Table 5

Conversions and products molar ratio after 1 h and 40 h of run in combined steam and dry reforming of methane ($\text{CH}_4/\text{CO}_2/\text{H}_2\text{O} = 1/0.4/0.8/12$, $T = 800 \text{ °C}$, $P = 1 \text{ atm}$); coke content on spent catalysts after 40 h of run. Data obtained at two different GHSV of 138 and $69 \text{ L g}_{\text{cat}}^{-1} \text{ h}^{-1}$ (using 50 and 100 mg of catalyst, respectively).

GHSV $\text{L g}_{\text{cat}}^{-1} \text{ h}^{-1}$	Catalyst	Conversion (%)				Molar composition of main products		Coke content (wt%) ^a
		t = 1h		t = 40h		t = 1h	t = 40h	
		X CH_4	X CO_2	X CH_4	X CO_2	H $_2/\text{CO}$	H $_2/\text{CO}$	
138	$\text{Ni}_5\%\text{Al}_2\text{O}_3$	57	51	59	54	2.12	2.17	9
138	$\text{Ni}_{7.5}\%\text{Al}_2\text{O}_3$	66	63	67	61	2.20	2.22	12
138	$\text{Ni}_{10}\%\text{Al}_2\text{O}_3$	81	79	82	77	2.27	2.33	19
138	$\text{Ni}_5\%\text{Ca}_5\%\text{Al}_2\text{O}_3$	64	58	65	58	2.09	2.05	4
138	$\text{Ni}_5\%\text{Mg}_5\%\text{Al}_2\text{O}_3$	79	73	80	74	2.10	2.10	3
69	$\text{Ni}_5\%\text{Al}_2\text{O}_3$	81	76	82	77	2.12	2.10	6
69	$\text{Ni}_{7.5}\%\text{Al}_2\text{O}_3$	85	81	87	81	2.11	2.16	7
69	$\text{Ni}_{10}\%\text{Al}_2\text{O}_3$	89	85	88	83	2.20	2.23	9
Thermodynamic values		92	87	92	87	2.10	2.10	16

^a Determined by TGA/DTA analyses of 40 h spent catalysts from the weight loss between 300 and 900 °C.

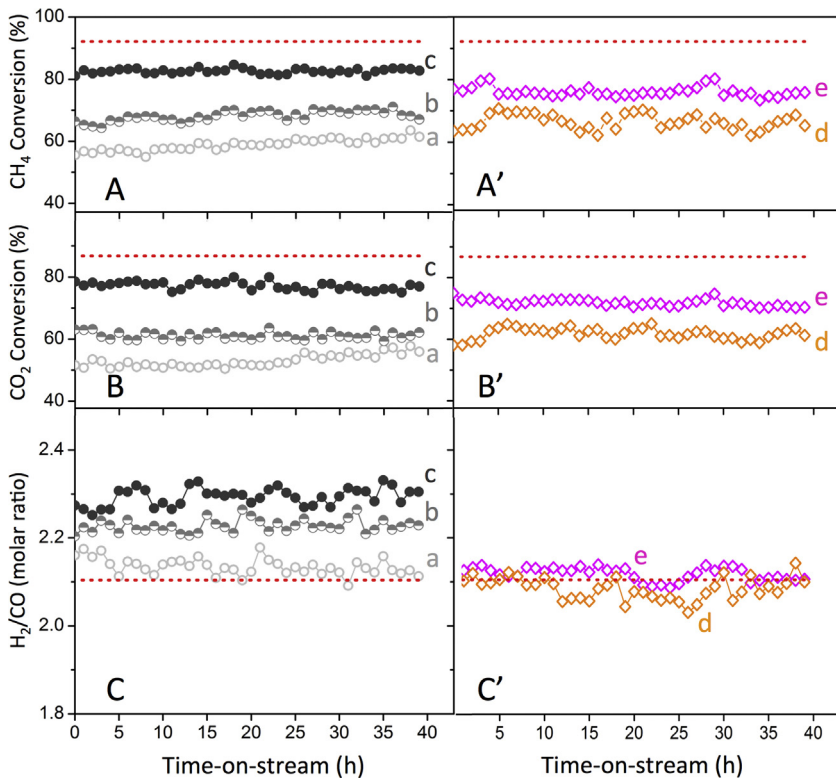


Fig. 5. (A,A') CH₄ conversions, (B,B') CO₂ conversions and (C,C') H₂/CO molar product ratio during combined steam and dry reforming of methane at 800°C (P=1 atm, GHSV=138 L g_{cat}⁻¹ h⁻¹) as a function of time-on-stream over: (a) Ni_{5%}Al₂O₃, (b) Ni_{7.5%}Al₂O₃, (c) Ni_{10%}Al₂O₃, (d) Ni_{5%}Ca_{5%}Al₂O₃ and (e) Ni_{5%}Mg_{5%}Al₂O₃ catalysts. Thermodynamic values (dashed-lines) were calculated with the HSC 7.1 Chemistry software.

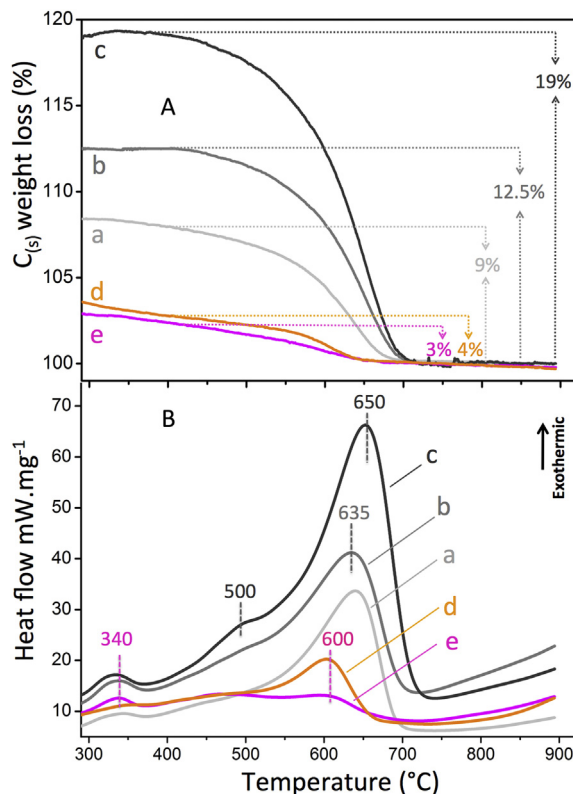


Fig. 6. (A) TGA and (B) DSC profiles of spent (800°C/40 h, CH₄/CO₂/H₂O/Ar = 1/0.4/0.8/12, GHSV = 138 L g_{cat}⁻¹ h⁻¹) catalysts: (a) Ni_{5%}Al₂O₃, (b) Ni_{7.5%}Al₂O₃, (c) Ni_{10%}Al₂O₃, (d) Ni_{5%}Ca_{5%}Al₂O₃ and (e) Ni_{5%}Mg_{5%}Al₂O₃.

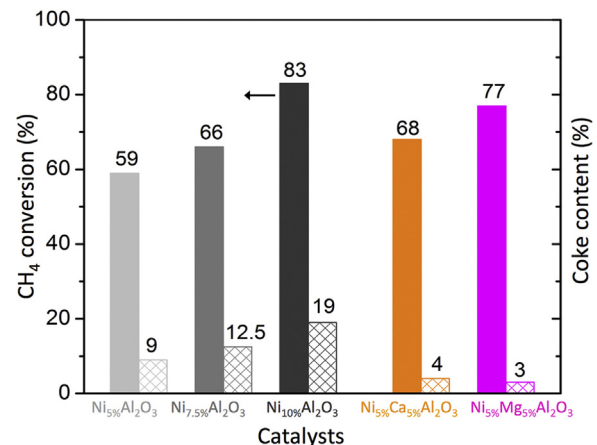


Fig. 7. Correlation between reactivity levels (mean methane conversion) and coke deposition (C_(s) wt%) along stability tests (800°C/40 h, CH₄/CO₂/H₂O/Ar = 1/0.4/0.8/12, GHSV = 138 L g_{cat}⁻¹ h⁻¹).

to the high reactivity of the samples, then it can be assumed that only part of the active sites participate to the catalytic act, which may reduce the contribution of side reactions compared to the main one (many active sites remaining available for CSDRM).

Coming back to the DSC profiles (Fig. 6B), the three distinct exothermic peaks reveal co-existence of at least three types of coke-derived species, currently described as (i) weakly stable amorphous C α (sp² C-atoms, superficial C or graphene-like species, peak 300–450°C), (ii) C β (C-nanotubes, peak 450–550°C) and (iii) stable crystalline C γ graphite (sp³ C-atoms, peak above 550°C) [63]. From the predominant high temperature signal seen for all spent Ni_xAl₂O₃ (curves a–b, Fig. 6B), it is tempting to conclude that carbon in these samples is mainly present in the form of C γ graphite.

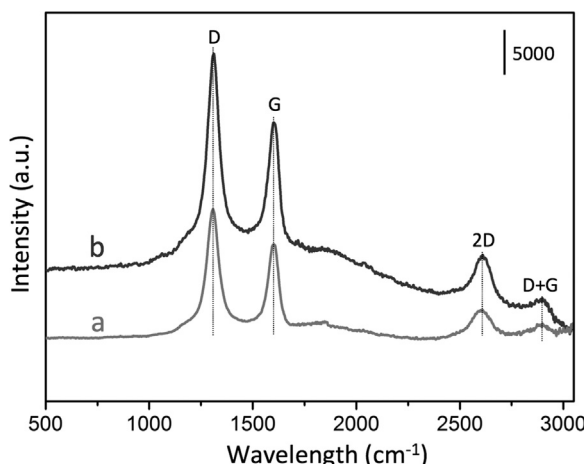


Fig. 8. Raman spectra of spent ($800^{\circ}\text{C}/40\text{ h}$, $\text{CH}_4/\text{CO}_2/\text{H}_2\text{O}/\text{Ar} = 1/0.4/0.8/12$, $\text{GHSV} = 138 \text{ L g}_{\text{cat}}^{-1} \text{ h}^{-1}$) catalysts: (a) $\text{Ni}_{7.5\%}\text{Al}_2\text{O}_3$ and (b) $\text{Ni}_{10\%}\text{Al}_2\text{O}_3$.

Nevertheless, such carbon family is known as the most inert type of coke, strongly contributing to deactivation by encapsulating the active sites and making them no longer accessible to gaseous reactants [64]. In view of the high catalytic stability of the samples (Figs. 5A–C), such poisoning effect seems unlikely. Rather, as already proposed in the literature [65–67], we assume that the high temperature oxidation peak corresponds to less toxic transitory intermediate carbon species formed during gradual transformation of reactive $\text{C}\alpha$ and/or $\text{C}\beta$ into $\text{C}\gamma$. These species could be analogous to carbon nanotubes previously reported to form on nickel impregnated alumina during DRM without necessarily leading to catalyst deactivation [68], as will be indeed confirmed below by Raman, XRD and TEM/SEM data. The high temperature DSC peak almost vanished for both spent $\text{Ni}_{5\%}\text{Mg}_{5\%}\text{Al}_2\text{O}_3$ and $\text{Ni}_{5\%}\text{Ca}_{5\%}\text{Al}_2\text{O}_3$ catalysts (curves d and e, Fig. 6B), in accordance with their very small $\text{C}_{(\text{s})}$ content, and the peak slightly shifted towards lower temperature. Again, this is most probably due to the dynamic character (heating) of the analysis (as for TPR, see Section 3.1), the maximum of the process (here an oxidation) occurring at slightly lower temperature when a lower amount of compound to be transformed is concerned. This is verified as well with the $\text{Ni}_{x\%}\text{Al}_2\text{O}_3$ series of samples having varying coke contents (curves a–c, Fig. 6B). More remarkably, a low DSC temperature peak is distinctly identified for $\text{Ni}_{5\%}\text{Mg}_{5\%}\text{Al}_2\text{O}_3$ (and for $\text{Ni}_{5\%}\text{Ca}_{5\%}\text{Al}_2\text{O}_3$ to a lesser extend) in spite of the overall weak signal intensity (curve e, Fig. 6B), revealing carbon deposition mainly as non-poisoning amorphous $\text{C}\alpha$ in this sample bearing a basicity promoter additive.

The transitory amorphous (rather than highly crystalline) state of carbon deposits in the $\text{Ni}_{x\%}\text{Al}_2\text{O}_3$ catalysts was also confirmed by Raman spectroscopy. Exploitable signals were obtained only for the spent $\text{C}_{(\text{s})}$ richest $\text{Ni}_{7.5\%}\text{Al}_2\text{O}_3$ and $\text{Ni}_{10\%}\text{Al}_2\text{O}_3$ catalysts, otherwise the carbon species were not entirely covering the alumina particles and a strong fluorescence background, as often observed with microporous zeolites [69] or mesoporous silica or alumina [70] was hampering correct data detection. The two main bands in the spectra (Fig. 8) were typical of the doubly degenerated phonon mode of C atoms in sp^2 carbon networks with high degree of symmetry and of order (graphitic carbon, G-band, 1601 cm^{-1}) and of a disordered structural mode of carbon species (D-band, 1312 cm^{-1}) [71–73]. The intensity ratio between these two bands (I_D/I_G) is often used as an indicator of the crystalline degree and/or presence of defects in the carbon species, the smaller the ratio (less than 1) the higher the structural order [71,73]. The ratio significantly higher than unity for both spent $\text{Ni}_{7.5\%}\text{Al}_2\text{O}_3$ and $\text{Ni}_{10\%}\text{Al}_2\text{O}_3$ (1.53 and 1.52, respectively) supports the assumption of the disordered

(rather than well-ordered crystalline graphitic) character of the carbon deposits. This is also in accordance with the peaks at circa 2700 and 2900 cm^{-1} (labeled 2D and (D+G) bands, respectively, Fig. 8) that were recently reported, for poorly crystalline carbon containing samples (with $I_D/I_G = 1.05$), to provide further evidence of the presence of disorder and/or of defects in the carbon sp^2 species [74].

3.6. Morphological aspects and preservation of Ni dispersion during reaction

The shape of the coke deposits was next identified by electron microscopy that also provided important information on the morphology of porous networks and on nickel dispersion and location in the spent catalysts. Typical SEM (Figs. 9A,B) and TEM (Figs. 9C,D) images are shown for spent $\text{Ni}_{10\%}\text{Al}_2\text{O}_3$ taken as most representative (Ni-richest and $\text{C}_{(\text{s})}$ -richest) material. In this sample, long-carbon filaments are clearly identified (detected by both SEM and TEM) on the external surface of the alumina-based grains, some grains appearing slightly more covered than others. Ni nanoparticles developing coke are also visible, located either at the interface between the support and the grown filament or embedded into it. In some case, a peculiar “bamboo shape” due to the formation of several adjacent compartments can be recognized. This resembles the reported nucleation of carbon nanotubes with “close end” having a nanoparticle either at their bottom or within their tip [67,68,75].

Notably, the diameter of the carbon nanowires is close to that of the metal particles on which they grew, the nanoparticle being itself sintered compared to the nanoparticles that are still occluded inside the walls or the pores of alumina. This is a strong argument in favour of a main participation of external metal nanoparticles to the growth of carbon nanotubes, some Ni^0 particles thus suffering of simultaneous sintering and encapsulation in carbon species during the run. Nevertheless, they appear much less numerous, by far, than the highly dispersed Ni^0 nanoparticles remaining occluded within the mesopores of the alumina-based network (Figs. 9C,D and Fig. 10).

From microtome TEM images, it is clear that the uniform channel system and its ordered hexagonal organization (porous network) is quite well preserved, both along $[1\ 1\ 0]$ (Figs. 10A, B, B') and perpendicular to $[0\ 0\ 1]$ (Figs. 10A', C, C') grain directions, even after 40 h run at 800°C under reactants (including steam). This excellent structural resistance is also attested by the N_2 -sorption data of spent $\text{Ni}_{10\%}\text{Al}_2\text{O}_3$ (taken as example) after its re-calcination at 800°C for coke removal (Fig. 11) and by the persistence of low angles XRD peaks in the patterns for all spent catalysts (Fig. 12A). From sorption data, some textural collapse is noted after reduction (curve b, Fig. 11), accentuated after catalysis (curve c, Fig. 11), but the spent catalyst still exhibits a well-defined type IV isotherm. This collapse could be related to a phase transition of the alumina substrate from mainly amorphous to more crystalline γ -phase as suggested by the XRD patterns of reduced and spent catalysts (Fig. 12B) where peaks typical of crystalline $\gamma\text{-Al}_2\text{O}_3$ are visible, whatever the sample. This indicates a transition from amorphous into crystalline γ -alumina of (at least part of) the alumina phase at the high temperatures applied (800°C), and the phenomenon is slightly accentuated after catalysis (patterns b'-d', Fig. 12B) in line with longer heating treatment. Note, however, the absence of any intense and thin XRD peak (and therefore absence of formation of a bulky crystalline phase), which reveals a satisfying structural resistance of the organized alumina-based networks, in spite of the drastic conditions of reaction. Thus, the loss in surface area and pore volume (values in Table 2) are of about 15% (after reduction) and 50% (after catalysis) but the pore size distributions remain unchanged. The collapse would therefore consist more in a progressive blocking of part of the pores rather than in a general shrinkage of the channels. In spite of such textu-

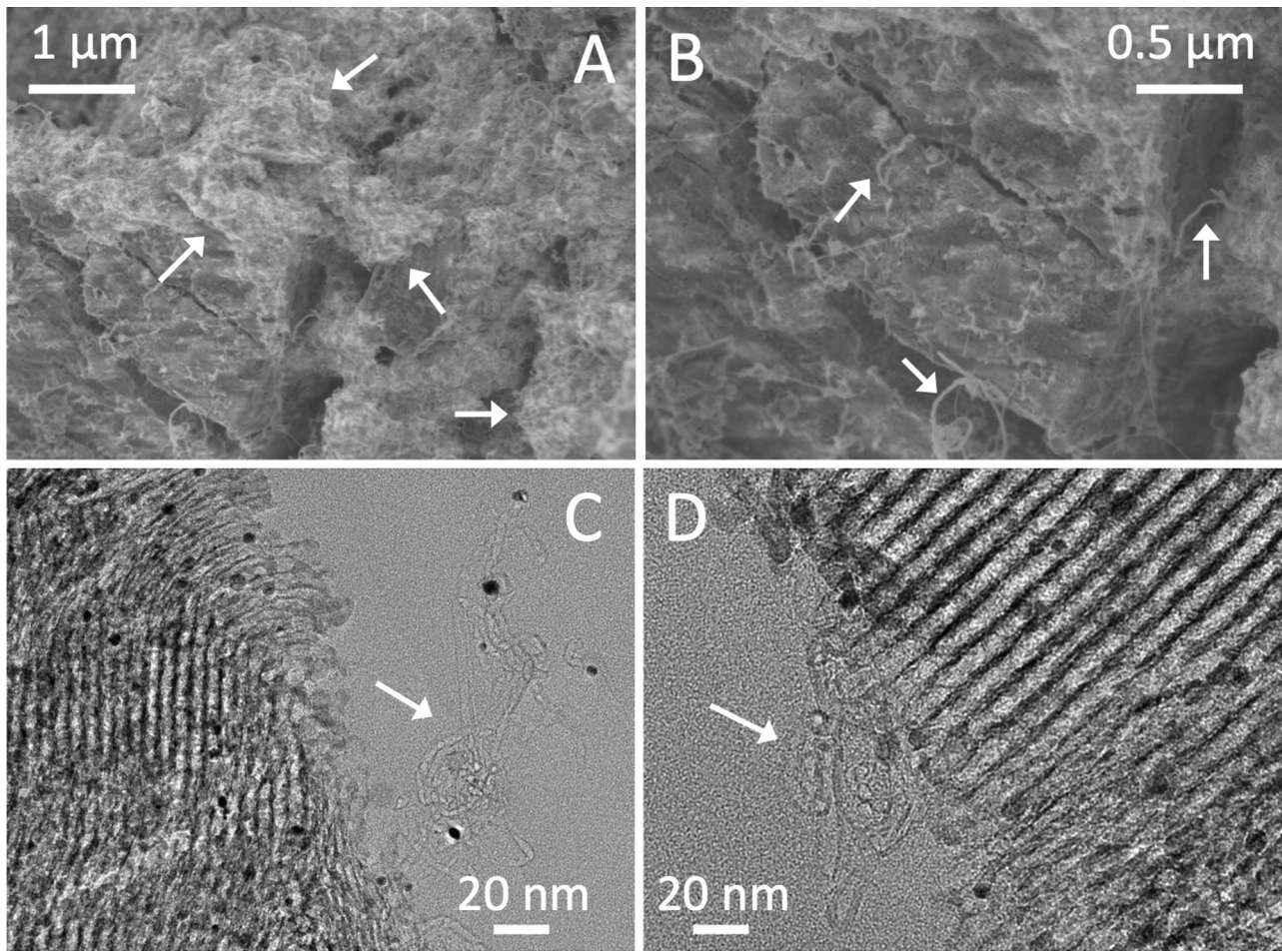


Fig. 9. (A,B) SEM and (C,D) TEM micrographs of spent ($800^{\circ}\text{C}/40\text{ h}$, $\text{CH}_4/\text{CO}_2/\text{H}_2\text{O}/\text{Ar} = 1/0.4/0.8/12$, $\text{GHSV} = 138 \text{ L g}_{\text{cat}}^{-1} \text{ h}^{-1}$) $\text{Ni}_{10\%}\text{Al}_2\text{O}_3$. Some carbon deposits are marked with arrows.

ral loss, many pores (half of initial ones after $800^{\circ}\text{C}/40\text{ h}$ reaction) remain open and accessible to reactants.

The other remarkable information resides in the numerous tiny Ni^0 nanoparticles that appear confined and well stabilized within the channels or even, in some cases, integrated within the alumina walls (Figs. 10B,B',C,C'). This reveals some nickel sintering during high temperature treatments, as also confirmed by the weak XRD peaks typical of fully reduced Ni^0 with face centered cubic (FCC) unit cell (ICDD file # 65-0380) that become detectable (indexed \star in Fig. 12B) after reduction (patterns a-f) and are only scarcely modified after catalysis (patterns b'-f'), showing that the metal nanoparticles remain stable during the run. The average sizes of the Ni^0 particles deduced from these signals are in accordance with those estimated from TEM data (Table 6). In spent $\text{Ni}_{10\%}\text{Al}_2\text{O}_3$, the nickel nanoparticles have a mean diameter around 7 nm (as estimated from particle size counting), much smaller than those commonly reported (above 20 nm) for Ni-impregnated alumina catalysts (even mesoporous ones) after CSDRM run [15,44]. The mean size is even smaller (5–6 nm) in the 5 wt% Ni containing catalysts, independently on the presence or not of Mg or Ca additive (Table 6). Such difference could be due to the total absence of sintered Ni^0 nanoparticles on the external surface of the alumina grains while few with sizes as high as 20 nm were detected in the Ni richest spent $\text{Ni}_{10\%}\text{Al}_2\text{O}_3$ (as exemplified in Fig. 10A).

Note also the absence of XRD signal attributable to graphitic deposits (expected around $2\theta \sim 29^{\circ}$), even for $\text{C}_{(s)}$ richest $\text{Ni}_{10\%}\text{Al}_2\text{O}_3$ (pattern d', Fig. 12B) that agrees with the negligible content of crystalline carbon in the spent catalysts deduced above

Table 6

Average particle size of nickel species in reduced (*in-situ* H_2 -reduction, $800^{\circ}\text{C}/3\text{ h}$) and spent ($\text{CH}_4/\text{CO}_2/\text{H}_2\text{O} = 1/0.4/0.8/12$, $800^{\circ}\text{C}/40\text{ h}$, $\text{GHSV} = 138 \text{ L g}_{\text{cat}}^{-1} \text{ h}^{-1}$) catalysts.

Samples	Reduced, $\varnothing \text{ Ni}^0(\text{nm})$		Spent, $\varnothing \text{ Ni}^0(\text{nm})$	
	XRD ^a	TEM	XRD ^a	TEM
$\text{Ni}_{5\%}\text{Al}_2\text{O}_3$	3.5	3.0 ^b	5.8	5.5 ^b
$\text{Ni}_{5\%}\text{Ca}_{5\%}\text{Al}_2\text{O}_3$	3.3	–	6.1	5.4
$\text{Ni}_{5\%}\text{Mg}_{5\%}\text{Al}_2\text{O}_3$	3.8	–	5.9	5.1
$\text{Ni}_{7.5\%}\text{Al}_2\text{O}_3$	4.7	–	6.5	–
$\text{Ni}_{10\%}\text{Al}_2\text{O}_3$	5.4	4.5	8.2	7.2

^a Calculated using Scherrer's equation at $2\theta = 51.8^{\circ}$ for the [200] indexed plane, n.d.: not determined (broad peaks).

^b From our previous work [ref. [15]].

from Raman data. Moreover, carbon deposits are not seen inside the preserved porous networks (TEM pictures).

3.7. Combined factors ensuring catalytic stability in CSDRM

From all above data, it can be concluded that the combination of “one-pot” synthesis (carried out in presence of Ni) with the “EISA” method (performed in presence of a structuring agent for generating ordered porosity) allowed to obtain, in a single step synthesis procedure, highly effective catalysts still exhibiting an organized mesoporous network and a highly dispersed Ni^0 active phase even after 40 h of CSDRM testing at 800°C under reactants. The “one-pot” methodology permitted to fully introduce nickel in the materials,

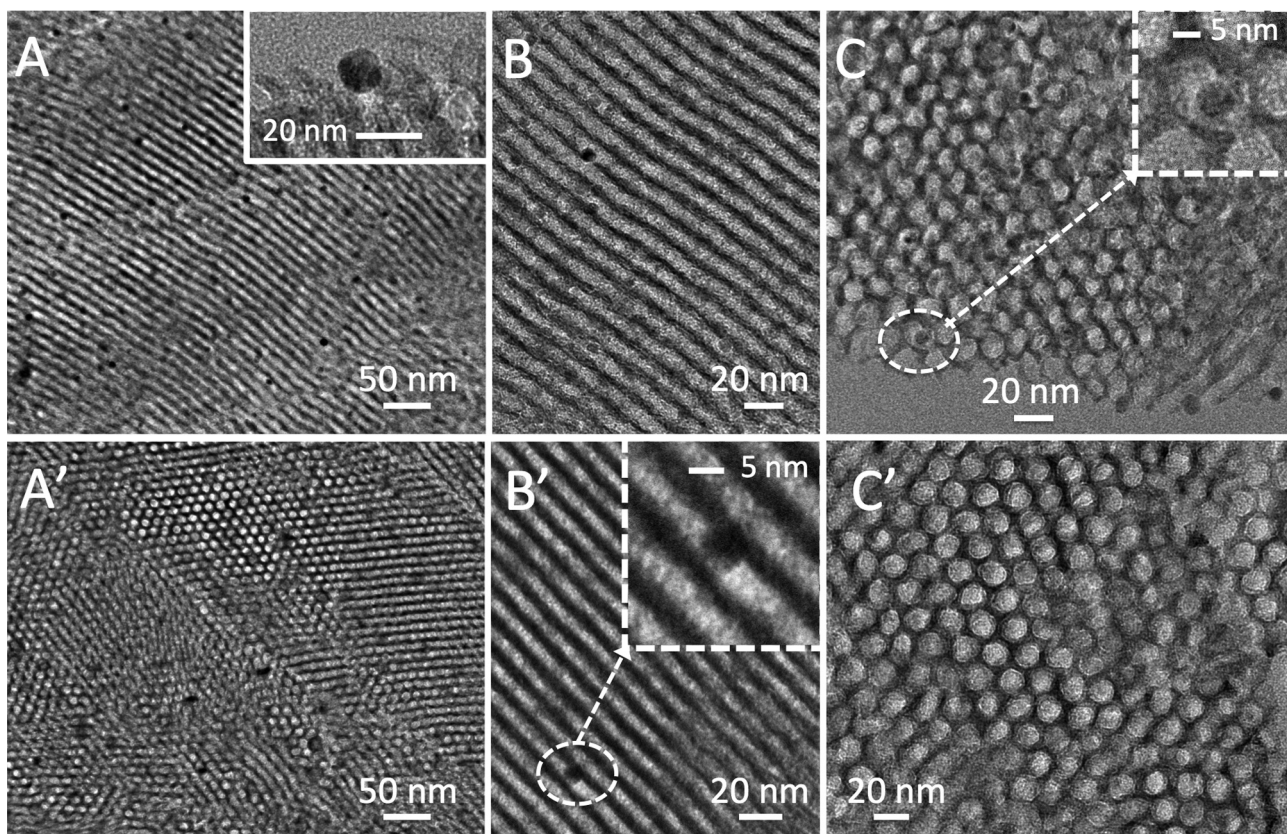


Fig. 10. TEM micrographs of spent ($800^{\circ}\text{C}/40\text{ h}$, $\text{CH}_4/\text{CO}_2/\text{H}_2\text{O}/\text{Ar} = 1/0.4/0.8/12$, $\text{GHSV} = 138\text{ L g}_{\text{cat}}^{-1}\text{ h}^{-1}$) (A–C) $\text{Ni}_{10\%}\text{Al}_2\text{O}_3$ and (A'–C') $\text{Ni}_{5\%}\text{Ca}_{5\%}\text{Al}_2\text{O}_3$ catalysts. Insets in Figures A, C and B' show zooms on the specified grain zones.

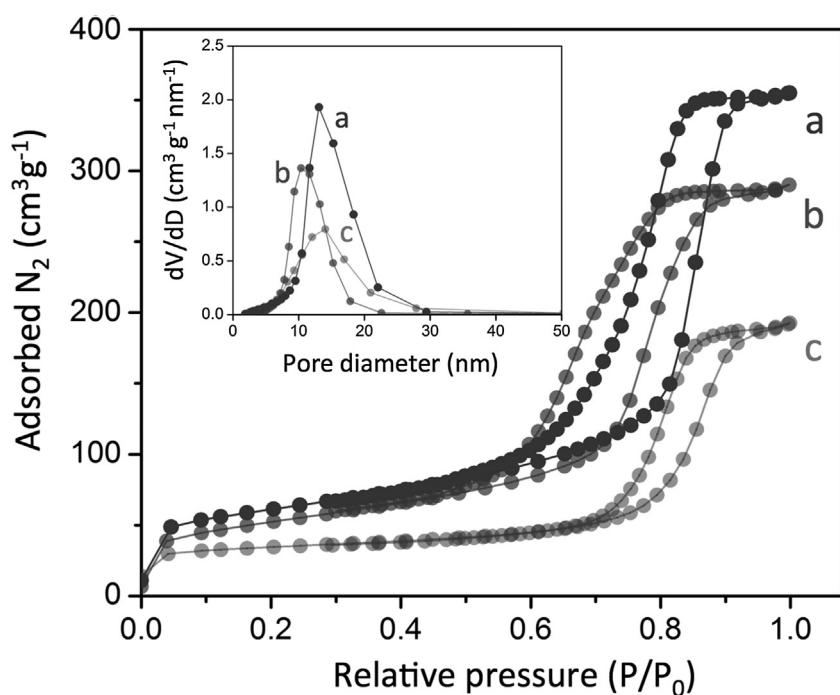


Fig. 11. N_2 -sorption adsorption-desorption isotherms and pore size distributions (inset) of (a) calcined, (b) reduced ($800^{\circ}\text{C}/3\text{ h}$) and (c) spent ($800^{\circ}\text{C}/40\text{ h}$, $\text{CH}_4/\text{CO}_2/\text{H}_2\text{O}/\text{Ar} = 1/0.4/0.8/12$, $\text{GHSV} = 138\text{ L g}_{\text{cat}}^{-1}\text{ h}^{-1}$) $\text{Ni}_{10\%}\text{Al}_2\text{O}_3$. Curve (c) was obtained after re-calcination ($450^{\circ}\text{C}/5\text{ h}$ in air) of the spent catalyst carried out in order to remove coke.

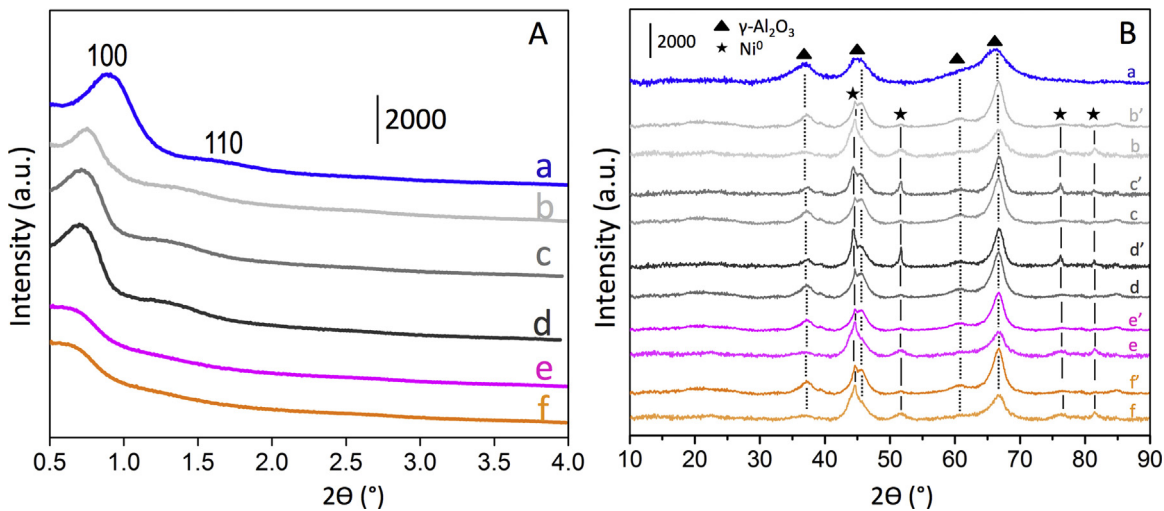


Fig. 12. (A) Low and (B) wide angles XRD patterns of (a–f) reduced ($800\text{ }^{\circ}\text{C}/3\text{ h}$) and (b'–f') spent ($800\text{ }^{\circ}\text{C}/40\text{ h}$, $\text{CH}_4/\text{CO}_2/\text{H}_2\text{O}/\text{Ar} = 1/0.4/0.8/12$, $\text{GHSV} = 138\text{ Lg}_{\text{cat}}^{-1}\text{ h}^{-1}$) catalysts: (a) Al_2O_3 , (b,b') $\text{Ni}_{5\%}\text{Al}_2\text{O}_3$, (c,c') $\text{Ni}_{7.5\%}\text{Al}_2\text{O}_3$, (d,d') $\text{Ni}_{10\%}\text{Al}_2\text{O}_3$, (e,e') $\text{Ni}_{5\%}\text{Ca}_{5\%}\text{Al}_2\text{O}_3$ and (f,f') $\text{Ni}_{5\%}\text{Mg}_{5\%}\text{Al}_2\text{O}_3$. An offset was applied along the Y-axis for the sake of clarity.

from the first step of their preparation, in the form of tiny species, possibly spinel-like ones, that are kept mainly embedded in the alumina-based walls after calcination at $450\text{ }^{\circ}\text{C}$ (not detected by XRD, neither by TEM, data to be published). Even if part (or all) nickel is extracted from the ordered oxide matrices during reduction (Ni^0 nanoparticles in the pores, as seen by TEM), the formed metal nanoparticles remain predominantly (if not fully) trapped inside the pores where they benefit of the surrounding oxide porous network that protects them against sintering. Notably, such confinement is also beneficial with respect to resistance of the reduced Ni^0 nanoparticles to re-oxidation (not detected in our spent catalysts). Comparable stability effects were recently claimed in the case of “one-pot” synthesized oxide-based catalysts tested in DRM [43,45,51,52,61] or in SRM [46], but such types of materials were never considered yet in the combined CSDRM reaction that involves much more drastic conditions (especially steam and high temperatures). Moreover, the present method introducing the active phase (Ni) and the structuring agent (P123 Pluronic triblock copolymer) in a same synthesis batch was, to our knowledge, never considered regarding nickel-alumina based mesoporous catalysts. Nevertheless, it provides confinement effects that appear to be key factors for ensuring the stability of the catalysts.

Even if the nickel-alumina based $\text{Ni}_{x\%}\text{Al}_2\text{O}_3$ catalysts already offer high activity levels (Table 5) and excellent stability (Fig. 5), the catalytic performances are further improved by adding an additive such as Mg (or to a lesser extend Ca). From the close Ni^0 nanoparticles sizes found in all 5 wt% Ni catalysts, whatever their composition (Table 6), it is clear that the additives do not play any role towards nickel dispersion or stabilization, as was already proposed [60]. Similarly, they have no beneficial effect in term of porous network stabilization since the materials show lower specific surface area and pore volumes than the analogous additive-free sample (Table 2). Rather, their positive impact on activity levels (Figs. 5 and 7, Table 5) resides in their propensity to provide some basicity (61) to the mixed additive-alumina-based oxide. This enhances CO_2 and H_2O activation and helps limiting the side reactions that can still occur at the high temperature of reaction, as seen from the enhanced selectivity towards metgas (molar H_2/CO product ratio close to 2, Fig. 5C') and from the drastic reduction of carbon contents in the spent catalysts (Figs. 6A and 7, Table 5). Note that the latter effect is important on an industrial point of view because carbon deposition is known to potentially lead to reactors blockage with time.

Table 7

Adsorption activated mechanisms (with successive steps) during DRM, SRM and CSDRM reactions [80].

Reaction type (and rate)	Mechanism	Equation number
CH_4 activation (R_I)	$\text{CH}_4 + 2* \rightarrow \text{CH}_2^* + *$	1
	$\text{CH}_2^* + * \rightarrow \text{CH}_2^* + \text{H}^*$	2
	$\text{CH}_2^* + * \rightarrow \text{CH}^* + \text{H}^*$	3
	$\text{CH}^* + * \rightarrow \text{C}^* + \text{H}^*$	4
H_2O activation (R_{II})	$\text{H}_2\text{O} + * \rightarrow \text{H}_2 + \text{O}^*$	5
CO_2 activation (R_{III})	$\text{CO}_2 + * \rightarrow \text{CO}_2^*$	6
	$\text{CO}_2^* + * \rightarrow \text{CO}^* + \text{O}^*$	7
	$\text{CO}^* \rightarrow \text{CO} + *$	8
	$\text{C}^* + \text{O}^* \rightarrow \text{CO} + 2*$	9
Surface reactions	$\text{CO}^* \rightarrow \text{CO} + *$	10
	$\text{H}^* + \text{H}^* \rightarrow \text{H}_2 + 2*$	11

The beneficial basicity effect can be understood by considering some mechanistic aspects already established for SRM and DRM on Ni, Ru, Rh, Pd, Ir and Pt based catalysts supported on magnesia [76]. It was proposed that these two reactions involve similar mechanisms and that reforming rates are essentially limited by C–H bond activation on metal (here Ni) surfaces, identified as an irreversible process contrarily to CO_2 and H_2O activations that are reversible [77–79]. Several activation elementary steps (Eq. (1)–(11)) were distinguished [77–80], which also stand for CSDRM. They involve the generation of adsorbed activated (i) carbon (C^* , succession of Eq. (1)–(4)), (ii) hydrogen (H^* , Eq. (2)–(4)), (iii) carbon monoxide (CO^* , Eq. (6) then (7)) and oxygen (O^* , Eq. (5) and (7)). These activated species next react together (Eq. (9)–(11)) to produce the expected gaseous CO and H_2 compounds. By facilitating H_2O and CO_2 dissociation [26,30,37], basicity enhances the formation of surface activated O^* that can then react with neighbour adsorbed C^* , thus inhibiting (or reducing) the participation of the latters to carbon polymerization phenomena that otherwise take place leading to coke [80]. In view of the high carbon contents in the spent $\text{Ni}_{x\%}\text{Al}_2\text{O}_3$ series of samples (Table 5), such coke deposits are formed at a significant extent in the less basic alumina-based materials (with no additives). This can be interpreted in term of a faster overall process of CH_4 decomposition and carbon polymerization (R_I , Table 7 and Fig. 13) compared to CO_2 and H_2O activation (R_{II} and R_{III} , respectively). By contrast, all reactions rates would be of the same order on more basic catalysts (Fig. 13). Remarkably, even when they exist at a significant amount, the coke deposits are only present as nanotubes grown on few external isolated (and sintered) Ni^0 nanoparticles

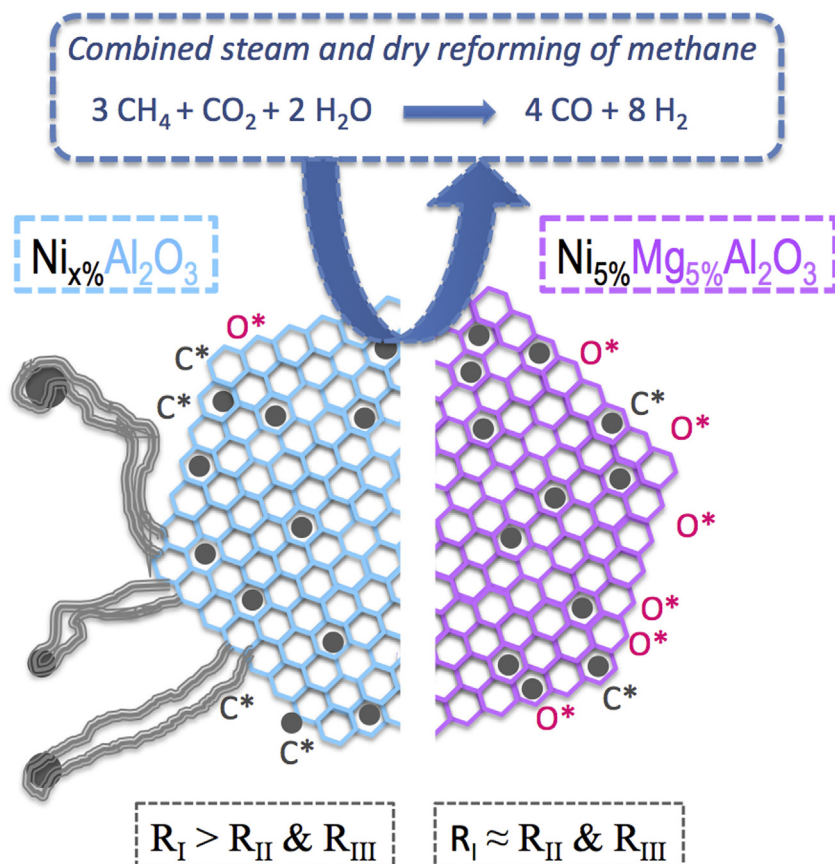


Fig. 13. Schematic representation of the spent catalysts. The CSDRM reaction takes place on the dispersed Ni^0 active nanoparticles remaining occluded (stabilized) in the preserved alumina-based mesoporous network. Adsorbed activated C^* and O^* species (formed upon dissociative adsorption of CH_4 , CO_2 and H_2O , Table 7) are also represented. The more numerous O^* on more basic catalysts (right hand side) react with neighbour adsorbed C^* leading to oxidative carbon removal ($R_I \approx R_{II}$ and R_{III}). On the contrary, rapid carbon polymerization takes place on less basic catalysts ($R_I > R_{II}$ and R_{III} , left hand side) resulting in the growth of carbon nanotubes on external Ni^0 nanoparticles that simultaneously suffer sintering.

located at the surface of the alumina grains (Fig. 9), and they are not detrimental to catalytic stability (Fig. 5) because they remain outside the pores, far away from the Ni^0 nanoparticles that are kept occluded inside the pores, still accessible and active towards the reactants (Fig. 10).

4. Conclusions

Ordered mesoporous nickel alumina (5–10 wt% Ni) materials eventually loaded with an additive (5 wt% Mg or Ca) were easily synthesized by a one-step procedure involving an evaporation-induced self-assembly strategy in presence of both an active phase (nickel) and a structuring agent. All nickel introduced in the synthesis medium was incorporated within the oxide matrix and this took place together with the structuration of the material in the form of well-organized channel networks. Upon reduction treatment needed to form the Ni^0 active phase, nickel is (at least partially) extracted from the alumina matrix but the nanoparticles remain predominantly (if not fully) occluded in the pores. The resulting high Ni^0 dispersion, together with a high resistance of the mesoporous network along 40 h of catalytic run at 800 °C under the harsh conditions of combined steam and dry methane reforming, appear as key factors leading to highly active and extremely stable catalysts. The catalytic performances are further enhanced by Mg (and to a lesser extent Ca) addition, but none of these two additives has an effect on structural features, neither on active phase dispersion. Rather, they play an effective role towards avoiding side reactions (nanotubes formation) and yielding high selectivity to metgas with

a stable H_2/CO molar product ratio kept close to 2 in the exhaust gas. In their absence, some side reactions take place, especially methane decomposition that leads to the formation of elongated carbon nanotubes, grown on one (or several) sintered Ni^0 particle, which are however weakly poisoning (no effect on catalytic stability) because they remain at the exterior of the alumina grains, far away from the numerous active Ni^0 nanoparticles confined in the pores. The beneficial effect of nickel confinement in the pores is therefore twofold, consisting in protecting the metal nanoparticles against sintering but also against coking in their neighbouring due to steric constraints. In view of their effective textural, structural and catalytic performances, the “one-pot” mesoporous catalysts presented in this study represent ideal candidates for catalyzing metgas (or more generally syngas) production from biogas and/or biomass natural resources.

Acknowledgments

Karam Jabbour sincerely acknowledge the “Agence Universitaire de la Francophonie” (AUF) and the Research Council of the University of Balamand for partial PhD funding (AUF fellowship and UOB 01/2013 BIRG, respectively). The authors are also sincerely grateful to (i) the French-Lebanese CEDRE Hubert Curien program (PHC) for financial support to mobility (project number 30962ZH, 2014–2015) and to (ii) the FP7 European program and related national organisms for SOL-CARE project funding (ERANETMED.ENERG-065, 2016–2019). Jean-Marc Kraft is thanked for his help in setting Raman instrumentation.

References

[1] J.D. Figueroa, T. Fout, S. Plasynski, H. McIvried, R.D. Srivastava, *Int. J. Greenh. Gas Control* 2 (2008) 9–20.

[2] W. Wang, S. Wang, X. Ma, J. Gong, *Chem. Soc. Rev.* 40 (2011) 3703–3727.

[3] G.A. Olah, G.S. Prakash, A. Goeppert, M. Czaun, T. Mathew, *J. Am. Chem. Soc.* 135 (2013) 10030–10031.

[4] G.A. Olah, A. Goeppert, M. Czaun, T. Mathew, R.B. May, G.K.S. Prakash, *J. Am. Chem. Soc.* 137 (2015) 8720–8729.

[5] G.A. Olah, A. Goeppert, M. Czaun, G.K.S. Prakash, *J. Am. Chem. Soc.* 135 (2013) 648–650.

[6] G.A. Olah, A. Goeppert, G.K.S. Prakash, *Beyond Oil and Gas: The Methanol Economy*, John Wiley and Sons, 2011.

[7] G.A. Olah, G.K.S. Prakash, US Pat. 2013, 8,440,729.

[8] G.A. Olah, G.K.S. Prakash, US Pat. 2014, 8,697,759.

[9] G.A. Olah, G.K.S. Prakash, US Pat. 2015, 8,980,961.

[10] G.A. Olah, G.K.S. Prakash, European Pat. 2010, 2,167,451A1.

[11] M.C.J. Bradford, M.A. Vannice, *Catal. Rev. Sci. Eng.* 41 (1999) 1–42.

[12] F. Pompeo, N.N. Nichio, M.V.M. Souza, D.V. Cesar, O.A. Ferretti, M. Schmal, *Appl. Catal. A* 316 (2007) 176–183.

[13] T.V. Choudhary, V.R. Choudhary, *Angew. Chem. Int. Ed.* 47 (2008) 1828–1847.

[14] M.S. Fan, A.Z. Abdullah, S. Bhatia, *ChemCatChem* 1 (2009) 192–208.

[15] K. Jabbour, N. El Hassan, A. Davidson, S. Casale, P. Massiani, *Catal. Sci. Technol.* 6 (2016) 4616–4631.

[16] D. Qin, J. Lapszewicz, X.J. Jiang, *Catalysis* 159 (1996) 140–149.

[17] D. Qin, J. Lapszewicz, J. Catal. Today 21 (1994) 551–560.

[18] M.A. Soria, C. Mateos-Pedrero, A. Guerrero-Ruiz, I. Rodríguez-Ramos, *Int. J. Hydrogen Energy* 36 (2011) 15212–15220.

[19] F. Yagi, A. Nagumo, Y. Wada, M. Shimura, US Pat. 2002, 6387843B1.

[20] S. Özkar-Aydinoglu, *Int. J. Hydrogen Energy* 35 (2010) 12821–12828.

[21] Y. Sun, T. Ritchie, S.S. Hla, S. McEvoy, W. Stein, J.H. Edwards, *J. Nat. Gas. Chem.* 20 (2011) 568–576.

[22] M. Jafarbegloo, A. Tarlani, A.W. Mesbah, S. Sahebdelfar, *Int. J. Hydrogen Energy* 40 (2015) 2445–2451.

[23] B.A. Santos, J.M. Loureiro, A.M. Ribeiro, A.E. Rodrigues, A.F. Cunha, *Can. J. Chem. Eng.* 93 (2015) 510–526.

[24] K.Y. Koo, H.S. Roh, Y.T. Seo, D.J. Seo, W.L. Yoon, S.B. Park, *Int. J. Hydrogen Energy* 33 (2008) 2036–2043.

[25] I.H. Son, S.J. Lee, A. Soon, H.S. Roh, H. Lee, *Appl. Catal. B* 134 (2013) 103–109.

[26] K.Y. Koo, H.S. Roh, Y.T. Seo, D.J. Seo, W.L. Yoon, S.B. Park, *Appl. Catal. A* 340 (2008) 183–190.

[27] H.S. Roh, K.Y. Koo, U.D. Joshi, W.L. Yoon, *Catal. Lett.* 125 (2008) 283–288.

[28] K.Y. Koo, H.S. Roh, U.H. Jung, W.L. Yoon, *Catal. Today* 185 (2012) 126–130.

[29] M. García-Díez, I.S. Pieta, M.C. Herrera, M.A. Larrubia, L.J. Alemany, *Catal. Today* 175 (2011) 136–142.

[30] J. Mehz, K.J. Jozani, A.N. Pour, Y. Zamani, *React. Kinet. Catal. Lett.* 75 (2002) 267–273.

[31] K.M. Kang, I.W. Shim, H.Y. Kwak, *Fuel Process. Technol.* 93 (2012) 105–114.

[32] K.Y. Koo, S.H. Lee, U.H. Jung, H.S. Roh, W.L. Yoon, *Fuel Process. Technol.* 119 (2014) 151–157.

[33] K.Y. Koo, H.S. Roh, U.H. Jung, D.J. Seo, Y.S. Seo, W.L. Yoon, *Catal. Today* 146 (2009) 166–171.

[34] S.C. Baek, J.W. Bae, J.Y. Cheon, K.W. Jun, K.Y. Lee, *Catal. Lett.* 141 (2011) 224–234.

[35] J.W. Bae, A.R. Kim, S.C. Baek, K.W. Jun, *React. Kinet. Catal. Lett.* 104 (2011) 377–388.

[36] A.N. Pour, Y.Z. Kheirolah, J. Jozani, J.Y. Mehr, *React. Kinet. Catal. Lett.* 86 (2005) 157–162.

[37] H.S. Roh, K.Y. Koo, J.H. Jeong, Y.T. Seo, D.J. Seo, Y.S. Seo, W.L. Yoon, S.B. Park, *Catal. Lett.* 117 (2007) 85–90.

[38] H.S. Roh, K.Y. Koo, W.L. Yoon, *Catal. Today* 146 (2009) 71–75.

[39] B. Huang, X. Li, S. Ji, B. Lang, F. Habimana, C. Li, *J. Nat. Gas Chem.* 17 (2008) 225–231.

[40] M.N. Kaydouh, N. El Hassan, A. Davidson, S. Casale, H. El Zakhem, P. Massiani, *Microporous Mesoporous Mat.* 220 (2016) 99–109.

[41] M.N. Kaydouh, N. El Hassan, A. Davidson, S. Casale, H. El Zakhem, P. Massiani, *C. R. Chim.* 18 (2015) 293–301.

[42] A. Albarazi, M.E. Gálvez, P. Da Costa, *Catal. Commun.* 59 (2015) 108–112.

[43] N. Wang, Z. Xu, J. Deng, K. Shen, X. Yu, W. Qian, W. Chu, F. Wei, *ChemCatChem* 6 (2014) 1470–1480.

[44] X. Fang, C. Peng, H. Peng, W. Liu, X. Xu, X. Wang, C. Li, W. Zhou, *ChemCatChem* 7 (2015) 3753–3762.

[45] L. Xu, H. Sonf, L. Chou, *Catal. Sci. Technol.* 1 (2011) 1032–1042.

[46] W. Shen, K. Komatsubara, T. Hagiya, A. Yoshida, S. Naito, *Chem. Commun.* 42 (2009) 6490–6492.

[47] S.M. Morris, P.F. Fulvio, M.M. Jaroniec, *J. Am. Chem. Soc.* 130 (2008) 15210–15216.

[48] Q. Yuan, A.X. Yin, C. Luo, L.D. Sun, Y.W. Zhang, W.T. Duan, H.C. Liu, C.H. Yan, *J. Am. Chem. Soc.* 130 (2008) 3465–3472.

[49] M.M. Naira, S. Kaliaguine, *New J. Chem.* 40 (2016) 4049–4060.

[50] F. Chen, C. Wu, L. Dong, A. Vassallo, P.T. Williams, J. Huang, *Appl. Catal. B* 183 (2016) 168–175.

[51] L. Xu, H. Song, L. Chou, *Appl. Catal. B* 108 (2011) 177–190.

[52] L. Xu, H. Song, L. Chou, *ACS Catal.* 2 (2012) 1331–1342.

[53] S.T. Harding, C.A. Floudas, *AIChE J.* 46 (2000) 1422–1440.

[54] W. Cai, J. Yu, C. Anand, A. Vinu, M.M. Jaroniec, *Chem. Mater.* 23 (2011) 1147–1157.

[55] A. Grosman, C. Ortega, *Langmuir* 24 (2008) 3977–3986.

[56] J. Zhang, H. Xu, X. Jin, Q. Ge, W. Li, *Appl. Catal. A* 290 (2005) 87–96.

[57] J.A.C. Dias, J.M. Assaf, *Catal. Today* 85 (2003) 59–68.

[58] S.Y. Chen, C.Y. Tang, J.F. Lee, L.Y. Jang, T. Tatsumi, S.J. Cheng, *J. Mater. Chem.* 21 (2011) 2255–2265.

[59] J. Rostrup-Nielsen, L.J. Christiansen, *Concepts in Syngas Manufacture* Imperial College Press, London, 2011.

[60] M. Nichele, V. Signoretto, F. Pinna, F. Menegazzo, I. Rossetti, G. Cruciani, G. Cerrato, A. Di Michele, *Appl. Catal. B* 150 (2014) 12–20.

[61] N. Wang, K. Shen, L. Huang, X. Yu, W. Qian, W. Chu, *ACS Catal.* 3 (2013) 1638–1651.

[62] J.M. García-Vargas, J.L. Valverde, J. Díez, P. Sánchez, F. Dorado, *Appl. Catal. B* 148 (2014) 322–329.

[63] J.Z. Luo, Z.L. Yu, C.F. Ng, C.T. Au, *J. Catal.* 194 (2000) 198–210.

[64] J. Guo, H. Lou, X.M. Zheng, *Carbon* 45 (2007) 1314–1321.

[65] Z.L. Zhang, X.E. Verykios, *Catal. Today* 21 (1994) 589–595.

[66] M.D. Argyle, C.H. Bartholomew, *Catalysts* 5 (2015) 145–269.

[67] L. Zhou, L. Li, N. Wei, J. Li, J.M. Bassett, *ChemCatChem* 16 (2015) 2508–2516.

[68] D. Chen, K.O. Christensen, E. Ochoa-Fernandez, Z. Yu, B. Tøtdal, N. Latorre, A. Monzon, A. Holmen, *J. Catal.* 229 (2005) 82–96.

[69] L.I. Meza, M.W. Anderson, J.R. Agger, C.S. Cundy, *From zeolites to porous MOF materials-The 40th anniversary of international zeolite conference, Proceedings of the 15th International Zeolite Conference* (2007).

[70] C.Y. Chen, H.X. Li, M.E. Davis, *Microporous Mater.* 2 (1993) 17–26.

[71] D. Liu, X.Y. Quek, W.N.E. Cheo, R. Lau, A. Borgna, Y. Yang, *J. Catal.* 266 (2009) 380–390.

[72] M. Che, J.C. Vedrine, *Characterization of Solid Materials and Heterogeneous Catalysts*, Wiley-VCH, 2012, pp. 64–67.

[73] C. Pan, Q. Bao, *J. Mater. Sci. Lett.* 21 (2002) 1927–1929.

[74] E.C. Vermisoglou, T. Giannakopoulou, G. Romanos, M. Giannouri, N. Boukos, C. Lei, C. Lekakou, C. Trapalis, *Appl. Surf. Sci.* 358 (2015) 100–109.

[75] T.V. Choudhary, E. Aksöy, D.W. Goodman, *Catal. Rev. Sci. Eng.* 45 (2003) 151–203.

[76] J.R. Rostrup-Nielsen, J.H. Bak Hansen, *J. Catal.* 144 (1993) 38–49.

[77] J. Wei, E. Iglesia, *J. Phys. Chem. B* 108 (2004) 4094–4103.

[78] J. Wei, E. Iglesia, *J. Catal.* 224 (2004) 370–383.

[79] A. Donazzi, A. Beretta, G. Groppi, P. Forzatti, *J. Catal.* 255 (2008) 259–268.

[80] T.H. Nguyen, A. Lamacz, A. Krzton, B. Liszka, G. Djéga-Mariadassou, *Appl. Catal. B* 182 (2016) 385–391.